Title: Aqueous dissolution of Li-Na borosilicates: insights from machine learning and experiments

Authors: Thomas L. Goût[1,*], Joseph N. P. Lillington[1], James Walden[1], Christina Boukouvala[1,2], Emilie Ringe[1,2], Mike T. Harrison[3], Ian Farnan[1]

[1]Department of Earth Sciences, University of Cambridge, Downing Street, Cambridge, CB2 3EQ, UK.

[2]Department of Materials Science and Metallurgy, University of Cambridge, 27 Charles Babbage Road, Cambridge, CB3 0FS, UK.

[3]National Nuclear Laboratory, Central Laboratory, Sellafield, Seascale, Cumbria, CA20 1PG, UK.

***Corresponding author:** T.L. Goût (tlg29@cam.ac.uk)

Declarations of interest: none

Keywords

Machine learning; Aqueous dissolution; Nuclear; Borosilicate glass; Nuclear magnetic resonance

Abstract

Previously acquired data could be utilised in predicting glass dissolution kinetics at long times, but the application of machine learning methods needs to be assessed. Here, the dissolution processes of two Li-Na borosilicate ‘base glasses’ at 40 and 90 °C were investigated by SEM-EDS, NMR and Raman spectroscopy. Boron and sodium machine learning predictions were excellent when considering other normalised releases as features. However, extrapolating the training feature space yielded poorer performance and the absence of incorporated waste

elements resulted in underestimated predicted long-term lithium and silicon releases. Faster dissolution kinetics were observed for MW than MW-½Li but the MW-½Li gel layer at 40 °C trapped more water. Whilst BO_3 rings leached preferentially at 90 °C, surface enrichment of BO_3 at 40 °C suggested $[BO_4]^-$ transformed prior to dissolution. Results were consistent with interdiffusion being significant at 40 °C and interface-coupled dissolution precipitation beyond 7 days at 90 °C.

1. Introduction

Quaternary mixed-alkali borosilicate glasses are of particular interest to the nuclear industry, being used in the UK as 'base glass frits' to which calcined high-level waste (HLW), arising from spent nuclear fuel reprocessing activities, is added during vitrification [1–6]. The Li-Na borosilicate base glass composition used for HLW vitrification in the UK, MW-½Li, and its original formulation, MW, are presented in Table 1. MW has an equimolar Li/Na ratio to optimise transport properties important to the vitrification process, such as melt viscosity, and its B contents provides a compromise between optimising waste loading, as limited by Mo solubility, and aqueous durability [7–10]. As the addition of $LiNO_3$ to the liquid waste improves its reactivity during calcination, half the molar Li of MW was removed (MW-½Li) to yield an equimolar Li/Na ratio in the final glass at a HLW loading of 25 wt.% [1,10].

Investigations which aim to constrain compositional and environmental effects on the dissolution of simulant HLW glasses are rendered difficult as the product HLW glasses typically comprise over 20 elements [11–14]. As such, simplified analogues are frequently used in mechanistic studies to better constrain these effects (*e.g.* [15–20]). In this view, dissolution experiments on MW and MW-½Li can provide valuable insights into the effects of varying the concentration of total alkalis (Li+Na) and the Li/Na ratio on pristine glass structure and dissolution behaviour without convoluting effects, such as complex altered layer structures and secondary phase precipitate assemblages. Indeed, in the absence of gel-forming species which require charge compensation, such as Al or Zr, alkali metals are solely removed from solution through secondary phase precipitation [21]. However, predicting compositional effects on chemical durability at long times remains a significant challenge in glass science [22].

Recent advances in machine learning (ML) techniques have led to significant improvements in the prediction of the physical properties of glasses, and can even automate the extraction of

these data from the literature (*e.g.* [23–30]). Analytical models often need to assume the mechanisms of glass dissolution (*e.g.* [31–33]), but these mechanisms have remained debated [22,34,35]. ML methods can make use of previously acquired data to predict dissolution behaviour without strictly being bound to assumptions of the underpinning mechanisms [36]. Indeed, decades of research have produced a large bank of experimental data on glass dissolution kinetics, with data-driven techniques such as ML presenting a potential means of making further use of these data in predicting future kinetics. Further, physics-informed ML can improve prediction accuracy and interpretability through using inflexible algorithms with physical constraints, such as glass network topology [37,38]. The successful application of ML methods to glass dissolution demands large datasets near-homogeneously spanning a diverse compositional and environmental feature space (*e.g.,* pH and temperature) [39]. However, ML has yet to successfully predict the long-term dissolution behaviour of simplified or complex HLW glasses solely from initial experimental conditions [40]. Rather, accurate predictions presently rely on the inclusion of pH and the concentrations of other non-response species as features [39,41].

Here, the dissolution behaviour of MW and MW-½Li was investigated by a combination of experimental and ML techniques. The aims of this study were to (1) investigate the performance of the ALTGLASS database (described in Section 2.5) [42,43] on comparatively simplistic glass compositions and dissolution conditions largely outside its feature space; (2) investigate the ability of ML to predict the dissolution behaviour of two compositionally similar glasses; and (3) deepen our understanding of the effects of simultaneously varying the Li/Na ratio and total alkali contents on the dissolution kinetics, secondary phase assemblages and altered layer structures of complex HLW glasses using comparatively simple base glasses as analogues.

77 The dissolution kinetics of MW and MW-½Li in static dissolution experiments in deionised
78 water at 40 and 90 °C were followed from 6 hours to 28 days, which may be considered a
79 standard timescale for short-term experiments (*e.g.* [11,44–46]). This dataset was then studied
80 further with ML techniques. Finally, differences in dissolution behaviour with composition and
81 temperature were then reconciled with glass structure, altered layer structures and secondary
82 phase assemblages through XRD, SEM-EDS (particle surfaces and cross-sections), NMR (^{11}B
83 and ^{23}Na SP MAS and ^{6}Li-^{1}H CP), Raman spectroscopy and geochemical modelling
84 (PHREEQC).

2. Experimental

2.1. Sample preparation and initial characterisation

MW and MW-½Li frits were initially synthesised in a 0.5 to 5.0 mm size fraction by James Kent Ltd (Stoke-on-Trent, UK). For all dissolution experiments, as-received glass frits were crushed in an agate mortar and pestle and sieved with stainless-steel sieves to a 75 to 150 µm size fraction. Powders were washed following an adaptation of the ASTM PCT washing procedure [47] solely using absolute ethanol to minimise prior exposure to water species before being dried at 90 °C for 16 hours. Secondary electron (SE) scanning electron microscope (SEM) images showed the particles were free from adhering fines (Figure S1). Particle size distributions of the prepared powders of were measured by laser diffraction (Malvern Mastersizer E) using an enclosed cell filled with absolute ethanol with 50 to 100 mg of sample. Distributions appeared uniform (Figure S2), with mean particle diameters of 121 ± 55 and 134 ± 65 µm (1 S.D.) for MW and MW-½Li, respectively. Glass densities were measured by Archimedes' principle with three to six replicates using ambient temperature deionised (DI) water. Measured densities agreed with laboratory-synthesised glasses presented in the literature (Table 1) [48,49].

2.2. Glass compositions

The nominal compositions of MW and MW-½Li are provided in Table 1 [1,7,49–52]. The Dell-Bray model predicts the fraction of B present in tetrahedral coordination, N_4, as a function of the glass K ($K = [SiO_2]/[B_2O_3]$) and R values ($R = [M_2O]/[B_2O_3]$, M = Li or Na) [53]. The model is briefly summarised as (1) $R \leq 0.5$, all added M_2O (M = Li, Na) converts BO_3 to $[BO_4]^- M^+$ to increase N_4; (2) $0.5 < R \leq 0.5 + K/16$, added M_2O continues to increase N_4 with the tetrahedral B units linking Si tetrahedra to form reedmergnerite groups (a B tetrahedron

connected to four Si tetrahedra); and (3) $0.5 + K/16 < R \leq 0.5 + K/4$, all alkalis form non-bridging oxygen (NBO) bonds with Si tetrahedra to increase Q^3 at the expense of Q^4 (Q^n is the fraction of Si tetrahedra with n bridging oxygen bonds) and N_4 remains constant with M_2O concentration. The Dell-Bray model predicts identical N_4 for both glasses, such that MW has a significantly larger estimated Q^3 than MW-½Li (Equation 1) [54–56].

$$Q^3 = \frac{2([M_2O]-N_4[B_2O_3])}{[SiO_2]} \qquad (1)$$

For compositional analyses, as-received MW and MW-½Li pieces were mounted in two-part epoxy resin (EpoFix, Struers) and polished using SiC papers and diamond pastes to 3 µm. Electron probe microanalysis (EPMA) was used to determine Si concentrations (Cameca SX100) using a beam diameter of 10 µm to analyse 70 spots on each sample, calibrating with a diopside standard. Concentrations of Li, B, and Na were determined by laser ablation inductively coupled plasma mass spectrometry (LA-ICP-MS; ESI NWR193^{UC} with Perkin-Elmer NexION 350D) using the EPMA SiO_2 concentration as the internal standard. Fifteen 2500 µm^2 squares were ablated per sample. NIST SRM 610, 612 and 614 and BCR-2G (USGS) were analysed as standards and international simple glass (ISG, MoSci) [2] as an in-house standard, as B is a trace element in NIST SRM 610 (350 µg g^{-1} [57]). Analysed compositions were within 10% of their nominal values with relative standard deviation (RSD) values < 5% (Table 1).

Table 1: Nominal and measured compositions (oxide mol.%), descriptors of the glass network and densities of MW and MW-½Li. Nominal compositions were compiled from literature data [1,7,49–52] *and nominal densities represent measured values for laboratory-synthesised glasses presented in the literature* [48,49]*. Compositions were determined by EPMA (SiO_2) and LA-ICP-MS (others) with associated uncertainties of 2% and 5%, respectively. Densities were determined by Archimedes' principle with uncertainties given as 1 S.D. Glass network descriptors were calculated as: $R = ([Li_2O] + [Na_2O])/[B_2O_3]$, $K = [SiO_2]/[B_2O_3]$* [48]*, Q^3 is calculated following Equation 1* [54]*, and $N_4 = 0.5 + K/16$* [53]*.*

	Nominal		Measured	
Oxide (mol.%)	**MW**	**MW-½Li**	**MW**	**MW-½Li**
Li_2O	10.5	5.6	10.8 ± 0.5	6.0 ± 0.3
B_2O_3	18.5	19.5	17.6 ± 0.9	20.5 ± 1.0
Na_2O	10.5	11.1	10.8 ± 0.5	10.9 ± 0.5
SiO_2	60.5	63.8	60.8 ± 1.2	62.7 ± 1.3
R (mol mol^{-1})	1.13	0.85	1.23	0.82
K (mol mol^{-1})	3.27	3.27	3.46	3.06
N_4 (calculated)	0.704	0.704	0.716	0.691
Q^3 (calculated)	0.26	0.09	0.30	0.09
Density (g cm^{-3})	2.47	2.45	2.47 ± 0.01	2.45 ± 0.09

2.3. Static dissolution experiments

Static dissolution experiments followed the ASTM PCT-B methodology [47]: 0.395 ± 0.005 g 75 to 150 µm MW and MW-½Li powders were leached in stainless-steel vessels with PTFE inserts using 4.0 ± 0.1 mL DI water (18.2 MΩ.cm at 25.0 °C) for a geometric glass surface area to solution volume ratio (S_{geo}/V) of 2150 ± 80 m^{-1}. The temperature was maintained at 40.0 and 90.0 ± 0.1 °C for 0.25, 1, 7, 14 and 28 days (Grant Instruments dry block heaters). Experiments took place in triplicate alongside four blank replicates.

Leachates were filtered using 0.45 µm nylon syringe filters (Whatman Puradisc). The pH(25°C) of samples aliquots were measured (Mettler Toledo LE438 pH electrode with FE20 FiveEasy pH meter; NIST traceable 4.00, 7.00 and 10.00 ± 0.01 pH buffers). Based upon triplicate sample pH measurements, a conservative uncertainty of ± 0.20 pH units was assigned to each average value. Glass powders were rinsed out of the reaction vessels with DI water and then dried at 90.0 ± 0.1 °C for 16 hours.

Leachates were analysed for Li, B, Na and Si concentrations by ICP optical emission spectroscopy (ICP-OES) (Agilent 5100) with SPS-SW2 (Spectrapure Standards) as a secondary standard. Detection limits were 0.03, 0.20, 0.06 and 0.10 μg mL^{-1} for Li, B, Na and Si, respectively, with RSD of ± 10% for the Li, B and Na concentrations and ± 20% to the Si concentrations based upon the measured recoveries of SPS-SW2 and sample replicate RSD. Measured sample concentrations were corrected for blank concentrations and leachant mass loss and used to calculate normalised elemental releases (Equation 2), where NL_i is the normalised elemental release of element i (g m^{-2}), C_i is the corrected concentration of i measured in solution (g L^{-1}), f_i is the elemental mass fraction of i in the pristine glass (unitless), S_{geo} is the geometric glass surface area (m^2) and V is the leachant volume (L) [47]. Note that S_{geo} is used rather than a measured specific surface area as the former corresponds more closely to the reactive surface area of the glass [58]. NL_B is used as a tracer of the extent of dissolution as B is not anticipated to be retained in the gel or incorporated into secondary phases in significant concentrations where the dissolution and subsequent transport of leached B species are not rate limiting [34,59].

$$NL_i = \frac{C_i}{f_i \frac{S_{geo}}{V}} \qquad (2)$$

NL_i uncertainties were propagated from the solution concentration measurements (± 20% Si, 10% others), elemental mass fractions (± 2% Si, 5% others) and the S_{geo}/V ratio (± 15%) following Equation 3 [60–62]; where $\hat{\sigma}$ is the relative uncertainty of the associated quantity and $\bar{C}_{i,b}$ is the average corrected blank concentration (g L^{-1}). The uncertainty associated with S_{geo}/V arises due to approximating the glass particles as spheres and is thought to represent a conservative overestimation [63,64]. Dissolution rates at time t, $r_{i,t}$ (g m^{-2} d^{-1}), can then be calculated as the first order derivative of NL_i with respect to time [65].

171 $$\hat{\sigma}_{NL_i} = \sqrt{\frac{(\hat{\sigma}_{Ci}C_i)^2+(\hat{\sigma}_{\bar{C}i,b}\bar{C}_{i,b})^2}{(C_i-\bar{C}_{i,b})^2} + \left(\hat{\sigma}_{f_i}\right)^2 + \left(\hat{\sigma}_{\frac{S_{geo}}{V}}\right)^2} \approx \sqrt{\left(\hat{\sigma}_{c_i}\right)^2 + \left(\hat{\sigma}_{f_i}\right)^2 + \left(\hat{\sigma}_{\frac{S_{geo}}{V}}\right)^2} \quad (3)$$

172 Equivalent altered layer thicknesses e_i (µm) were calculated from C_i, V and the mass of glass,
173 m (g), following the Shrinking Core model (Equation 4). e_i represents the altered glass
174 thickness required to produce the measured solution concentrations assuming spherical glass
175 particles of initial radius R_0 which are uniformly altered. That is, i is not retained [46,66,67].

176 $$e_i = R_0\left[1-\left(1-\frac{C_iV}{f_im}\right)^{\frac{1}{3}}\right] \quad (4)$$

177 Assuming e_{Si} represents the equivalent thickness due to network hydrolysis, $e_{\{B,Li,Na\}}$ - e_{Si}
178 represents the equivalent thickness due to interdiffusion [17]. Regressions where $NL_{\{B,Li,Na\}}$
179 evolve linearly with respect to $t^{0.5}$, hence where diffusion is assumed to significantly contribute
180 to the observed kinetics, can then be used to calculate apparent diffusivities, $D_{\{B,Li,Na\}}$, from the
181 glass density, ρ, using Fick's second law of diffusion following Equation 5 [46,65].

182 $$e_{\{B,Li,Na\}} - e_{Si} = \frac{NL_{\{B,Li,Na\}}-NL_{Si}}{\rho} = t^{\frac{1}{2}}\left[4\frac{D_{\{B,Li,Na\}}}{\pi}\right]^{\frac{1}{2}} \quad (5)$$

183

184 ## 2.4. Geochemical modelling

185 Geochemical modelling used leachate concentrations with PHREEQC (version 3) software
186 [68] with the ThermoChimie database (version 10a) [69], which had been modified to include
187 additional data on SiO_2 polymorphs, Na silicates and Li silicates from the LLNL database [70],
188 WATEQ4F database [71] and the literature [72] (additional phases described in Table S1).
189 These additional SiO_2 polymorphs and alkali silicates were considered based upon their
190 identification in previous studies [4,16,73,74]. Note that the magadiite data solely comprised a
191 log(K) value determined at 25 °C, without the thermodynamic data necessary for higher

192 temperature calculations. Calculations did not consider colloids but took place both with and
193 without assuming equilibrium between the solution and air (410 μmol mol^{-1} CO_2 and 209 mmol
194 mol^{-1} O_2 [75]).

195 The rate drop transition is controlled by the coupled processes of decreasing thermodynamic
196 affinity for dissolution and limited transport through the altered layer [76]. For the former, a
197 first-order rate law describes the dissolution rate at time t, r_t, as a function of affinity for
198 dissolution of the hydrated gel layer (Equation 6); where a*(H_4SiO_4) is an empirical parameter
199 denoting the activity of H_4SiO_4, $a(H_4SiO_4)$, at saturation with respect to the gel [77,78].
200 Assuming Li, B and Na are entirely leached from the gel [79], a*(H_4SiO_4) represents the
201 a(H_4SiO_4) at saturation with respect to amorphous silica, $(SiO_2)_{am}$ [13,64,80,81]. The time at
202 which dissolution evolves beyond this first-order rate law has been proposed as a quantitative
203 indicator of the start of the residual rate regime [16,82]. Here, the initial rate, r_0, was assumed
204 equal to the measured 6-hour B normalised release rate.

205 $$r_t = r_0 \left(1 - \frac{a_{H4SiO4}}{a^*_{H4SiO4}}\right) \qquad (6)$$

206

207 ## 2.5. Machine learning datasets and methodology

208 The ALTGLASS version 3 database [42,43] (version 4 is available [83]) was used in training
209 machine learning algorithms for predictions on the MW base glass data generated herein. This
210 database comprises 2636 observations from dissolution studies (ASTM PCT-A and PCT-B
211 [47]) on approximately 450 HLW and low activity waste (LAW) glass compositions, largely
212 in DI water at 90 °C, S_{geo}/V of 2000 m^{-1}.

213 Feature reduction was performed during data cleaning: features which were not applicable to
214 the dataset generated here, not applicable to predicting dissolution behaviour, weakly

correlated with the normalised releases or highly correlated with other features were removed. The removal of these features was also justified through examining the relative importance of features calculated using trained tree-based algorithms. Only experiments conducted in DI water were used in training and testing, such that leachant type was not used as a feature. Ultimately, the full set of features and responses included (range of ALTGLASS values excluding other leachant types provided in parentheses): time (0.42 to 7426 days), mass of glass leached (1.00 to 40.00 g), leachant volume (5.0 to 400.0 mL), S_{geo}/V ratio (1860 to 39100 m^{-1}), density (2.373 to 3.004 g cm^{-3}), temperature (90 to 200 °C), final leachate pH(25°C) (8.90 to 13.66), glass composition as elemental mass fractions (41 features, oxide wt.% compositions reported: 0.1 to 18.5% B_2O_3, 32.8 to 60.6% SiO_2, 0.0 to 7.91% Li_2O and 2.5 to 27.5% Na_2O) and $NL_{\{B,Li,Na,Si\}}$ (concentrations reported: 2.4 to 35230.6 µg mL^{-1} B, 11.4 to 45200.0 µg mL^{-1} Si, 0.0 to 6750.0 µg mL^{-1} Li and 8.0 to 76318.2 µg mL^{-1} Na). A heatmap of the correlations between features prior to feature reduction and histograms showing the positions of the base glass nominal compositions within the ALTGLASS compositional feature space are given in Figures S3 and S4, respectively.

Selected features were divided into subsets, with the response as either the normalised B, Li, Na or Si release to investigate whether accurate predictions of dissolution behaviour could be made from the experimental setup alone and what features were most related to the response. Feature subsets included: experimental features (time, mass of glass, glass mass fractions, glass density, leachant volume, S_{geo}/V ratio and temperature); experimental features and leachate pH; and experimental features, leachate pH and the other normalised releases not considered in the response (*e.g.,* Li, Na and Si releases as features with B release as the response).

The ML algorithms used herein ranged from inflexible linear models with excellent interpretability to more complex non-parametric models: linear regressions (LR: multiple, LASSO, Ridge, Elastic-net), support-vector machines (SVM: linear, polynomial and radial

basis function kernels), tree-based ensemble methods (gradient boosted, random forests and bagged random forests) and a single-layer feed-forward neural network (NN). Using a range of models varying in complexity affords an assessment of the model interpretability-complexity trade-off, allowing the simplest model possible to be selected to effectively describe the feature-response relationship.

In training and testing, the datasets were first divided into ALTGLASS and base glass data. Nested cross-validation (CV) [84,85] was then used to randomly partition the ALTGLASS database into independent training and test sets using a three-repeat five-fold CV method (outer CV), with algorithms being trained and their associated hyperparameters (variables used to control the learning process) being optimised using a five-fold CV method (inner CV) on the training set. Algorithm performance was assessed using the test folds of the outer CV (ALTGLASS data) and the base glass dissolution data to calculate average R^2 and CV estimates of the test mean squared error (MSE) (Equation 7) for each dataset separately; where y_i and $\hat{y}_i$ represent the measured and predicted response values of observation i, respectively, and n represents the number of observations in the dataset. The use of both R^2 and MSE provides a robust assessment of performance, with the former providing a standardised measure of overall model performance and the latter being more sensitive to outlying predictions.

$$MSE = \frac{1}{n}\sum_{i=1}^{n}(y_i - \hat{y}_i)^2 \qquad (7)$$

2.6. SEM-EDS and XRD

SEM images (FEI QEMSCAN 650F) and energy-dispersive X-ray spectroscopy (EDS) compositional maps were acquired for leached powders to investigate secondary phase assemblages and polished resin-mounted leached powders (pristine powders also resin-mounted and analysed as controls) to investigate altered layer structures. Resin-mounted samples were prepared and polished to a 0.25 μm finish using absolute ethanol lubricant to

avoid interactions with water. SE images were acquired under high vacuum (10^{-3} to 10^{-4} Pa) using an Everhart-Thornley detector (ETD) with a 2 to 5 kV beam, spot size of 1 to 3 and working distance of 5.0 to 7.5 mm. Backscattered electron (BSE) images and EDS maps were acquired under low vacuum (10^{-2} Pa) using a CBS detector and Bruker XFlash 6 | 30 silicon drift detectors, respectively, with a 20 kV beam, spot size of 4 and working distance of 13.0 mm, with maps being acquired for 10 to 30 minutes.

X-ray powder diffraction (XRD) (Bruker D8 Advance, Cu K_α source) took place on the pristine and 28-day leached powders. A Si low background sample holder was used to analyse approximately 20 mg powder from 3 to 60 ° (2θ) with a 0.05 ° step size and 7 s dwell per step (7980 s run time). XRD confirmed that the pristine glasses were amorphous (Figure S5).

2.7. Solid-state NMR experiments and quantification

All experiments were carried out with double resonance magic-angle spinning (MAS) probes using either a Varian Infinity Plus NMR spectrometer with 11.74 T magnet or Varian Infinity NMR spectrometer with 9.39 T magnet.

^{11}B MAS-NMR experiments at 160.32 MHz (11.74 T) used 15 to 20 mg of pristine sample and 85 to 120 mg of 28-day leached sample in 2.5 mm and 4.0 mm zirconia rotors, respectively, spun at 10.0 ± 0.1 kHz using a double resonance MAS probe. Single-pulse (SP) spectra were acquired using a 0.4 μs pulse (π/15) with a 6 s recycle delay for 240 to 256 repetitions. Spectra were referenced to solid $NaBH_4$ at -42.06 ppm. The ratio of ^{III}B (BO_3) to ^{IV}B ($[BO_4]^-$) units was quantified through fitting the spectra (dmfit software [86]) with four peaks: two for ^{III}B ring and non-ring resonances using literature NMR parameters [87–90], and two pseudo-Voigt peaks for the ^{IV}B peak unit reedmergnerite-like (4Si,0B) and danburite-like (3Si,1B) next-nearest neighbour contributions [90,91]. A first-order spinning sideband manifold was fitted to

subtract the contribution of the satellite transition spinning sidebands from the ^{IV}B signal from the central transition intensities [92].

^{23}Na MAS-NMR experiments at 132.18 MHz (9.39 T) used 80 to 120 mg of pristine or 28-day leached sample. Spectra were acquired during SP experiments with 4.0 mm zirconia rotors spun at 10.0 ± 0.1 kHz, a pulse width of 1.2 μs (π/15) and a recycle delay of 6 s for 900 to 1500 repetitions, referencing to 0.1 M NaCl in DI water at 0.0 ppm. Peak fitting (Igor Pro, Wavemetrics) first fitted the pristine spectra with a Lorentzian peak and an exponentially modified Gaussian peak to account for the quadrupolar lineshape (both peaks were interpreted identically). Fixed peak positions were then used to fit the leached spectra with an additional Lorentzian peak. A similar peak observed during simplified glass dissolution under similar conditions was concluded to correspond to a higher symmetry Na environment [93]. In turn, the intensity of this pristine peak was corrected for contributions from the (±1/2↔±3/2) transitions as only the (-1/2↔+1/2) transitions were observed for the pristine glass [94].

Static ^{6}Li-^{1}H CP-NMR experiments used 130 mg of the pristine glass without drying to confirm the absence of a signal from adsorbed water and the 28-day 90 °C samples. Analysis at 73.54 MHz for ^{6}Li and 499.72 MHz for ^{1}H (11.74 T) used 7.5 mm silicon nitride rotors with PTFE inserts. Spectra were acquired using 84500 to 125000 repetitions with an 8 μs pulse on ^{1}H (π/2) and a recycle delay of 3 s, referencing to 1.0 M $^{6}LiCl$ in DI water at 0.0 ppm.

2.8. Raman spectroscopy

Raman spectroscopy was used to analyse the pristine and 28-day leached samples. Powders were deposited onto an Al foil substrate to minimise the associated background signal. A Horiba LabRam 300 spectrometer was used with a 532 nm excitation laser through a 50x lens with 600 mm^{-1} grating to analyse over the 150 to 2000 cm^{-1} range. Three positions were analysed per sample with 10 accumulations per position, using an incident power of 100 or

250 mW with 90 or 40 s exposure time for MW and MW-½Li, respectively. ‘Rough’ and ‘smooth’ surfaces were observed for 90 °C MW, and so both regions were analysed in triplicate. Given the rough particle topography, spectra were interpreted qualitatively.

316 # 3. Results

317 ## 3.1. Dissolution kinetics

318 Sample concentrations were significant from the limits of quantification (< 0.5 μg mL^{-1} for all
319 species) and were greater than 10 S.D. above their respective mean blank concentrations
320 (< 0.60 μg mL^{-1} for Li, B and Na, and <3.25 μg mL^{-1} for Si). RSD values were less than 20%
321 for Si and 10% for all others. SPS-SW2 recoveries were within 10% (note Li is absent).
322 Measured NL_i and the corresponding ML predictions are presented in Figure 1.

323 At 90 °C, $NL_{B,Li,Na}$ for MW and MW-½Li increased with time up to 7 days before plateauing.
324 The NL_B of MW were consistently higher than MW-½Li, with 28-day leached B fractions and
325 estimated altered layer thicknesses for MW-½Li of 21.9 ± 4.1% and 4.5 ± 0.8 μm, respectively,
326 and 39.8 ± 7.4% and 8.8 ± 1.6 μm for MW, respectively. Similarly, the NL_{Li} was higher for
327 MW except at 1 and 14 days. However, the NL_{Na} of MW and MW-½Li were within uncertainty
328 until 28 days. At 90 °C the NL_{Si} reached steady state concentrations of 1567.0 ± 393.0 μg mL^{-1}
329 after 7 days and 514.5 ± 129.0 μg mL^{-1} before 6 hours for MW and MW-½Li, respectively.
330 This somewhat contrasts with literature results that the leached fraction of Si is largely
331 unaffected by increasing the [Na+B] concentration for Na borosilicates [95].

332 At 40 °C, the $NL_{B,Li,Na}$ increased near-linearly with time (linear regressions yielded
333 $R^2 \geq 0.9180$), with a considerably more modest slowing of the dissolution rate with time than
334 at 90 °C. The $NL_{Na,Li}$ of MW and MW-½Li remained within uncertainty throughout
335 dissolution, whilst the NL_B of MW was higher from 7 days onwards. This corresponded to 28-
336 day leached B fractions and estimated altered layer thicknesses for MW-½Li of 11.3 ± 2.1%
337 and 2.2 ± 0.4 μm, respectively, and for MW of 16.9 ± 3.2% and 3.4 ± 0.6 μm, respectively.
338 Steady-state Si concentrations were attained after 7 days at 186.7 ± 46.8 μg mL^{-1} and 445.3 ±
339 111.7 μg mL^{-1} for MW-½Li and MW, respectively. Whilst differences in dissolution kinetics

between MW and MW-½Li were more apparent at 90 °C, the ratios of the 90 °C $NL_{B,Li,Na}$ to the 40 °C $NL_{B,Li,Na}$ were within uncertainty for MW and MW-½Li throughout dissolution.

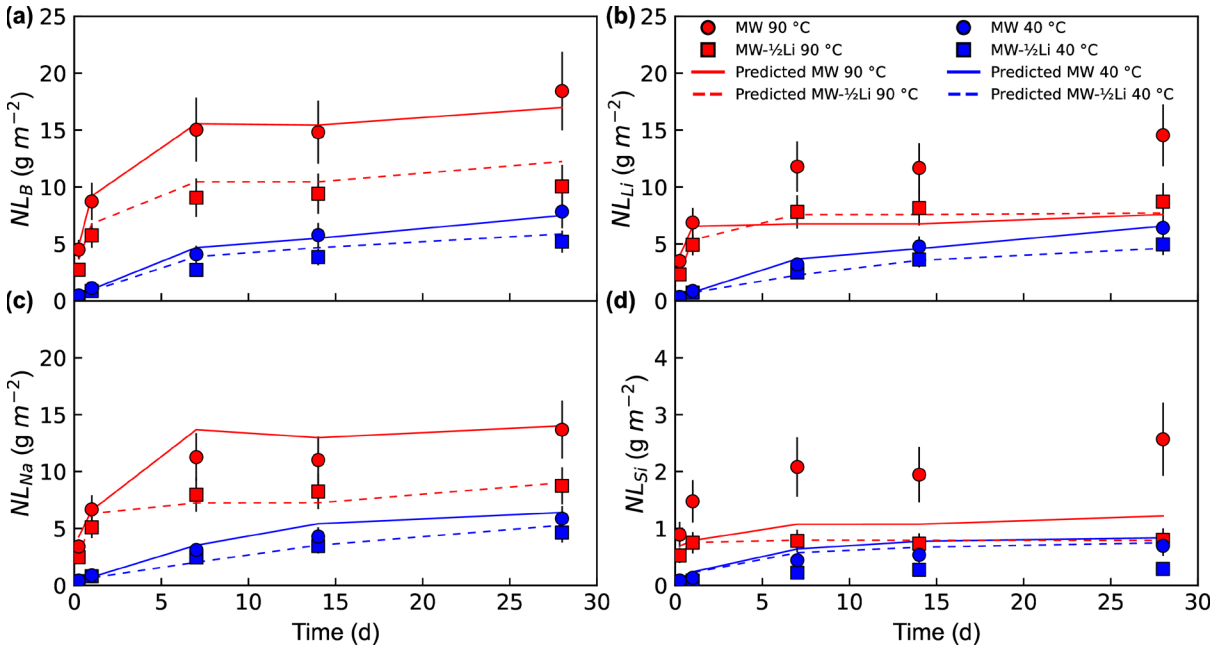

Figure 1: Measured normalised B (a), Li (b), Na (c) and Si (d) releases (markers) alongside ML predictions (lines). Predictions were made using a bagged random forest algorithm which considered all available features except the response release. Uncertainties are given to 1 S.D. (propagated using Equation 3) and range from 15 to 30% (RSD).

Assuming NL_{Si} is the contribution of Si network hydrolysis to $NL_{B,Li,Na}$, $NL_{B,Li,Na} - NL_{Si}$ represents the normalised releases through B hydrolysis or ion-exchange (Li,Na) ahead of the Si hydrolysis front [46,65]. In turn, diffusive processes can be assumed to contribute to the releases where $NL_{B,Li,Na} - NL_{Si}$ evolves linearly with respect to $t^{0.5}$, allowing for apparent diffusivities, $D_{B,Li,Na}$, to be extracted by linear regression using Equation 5 [17,82]. The $NL_{B,Li,Na} - NL_{Si}$ at 40 °C evolved linearly ($R^2 \geq 0.9970$) with $t^{0.5}$ at all durations (Figure 2), consistent with a single $D_{B,Li,Na}$ of the order 10^{-18} m^2 s^{-1} at the timescales studied (Table 2). Notably, at 40 °C all MW $D_{B,Li,Na}$ exceeded those of MW-½Li despite the $NL_{Li,Na}$ for all durations and NL_B up to 7 days being within uncertainty (Figure 1), consistent with differences in diffusion rates relative to hydrolysis for these glasses.

The 90 °C $NL_{B,Li,Na} - NL_{Si}$ evolved linearly with $t^{0.5}$ up to 7 days before plateauing to a constant value. This behaviour is also reflected in the $R^2 \geq 0.9375$ up to 7 days, with $D_{B,Li,Na}$ of the order

10^{-17} to 10^{-18} m^2 s^{-1}. Beyond 7 days, $D_{B,Li,Na}$ could not be obtained. This is consistent with a significant change in the dominant release mechanism of these species. Further, the MW $D_{B,Li,Na}$ were approximately twice those of MW-½Li. The orders of magnitude of the D_B agree well with those previously reported for Na-Ca-Al borosilicates of 1.7×10^{-17} m^2 s^{-1} (90 °C, 20 m^{-1}, 28 days in DI water) [96] and Na-Al borosilicates of 9×10^{-18} m^2 s^{-1} (90 °C, 2000 m^{-1}, 150 days, pH 7) [21], but are significantly higher than those reported for Na borosilicates during the residual rate of 2.6×10^{-19} m^2 s^{-1} (90 °C, 8000 m^{-1}, 2200 days in DI water) [16,17].

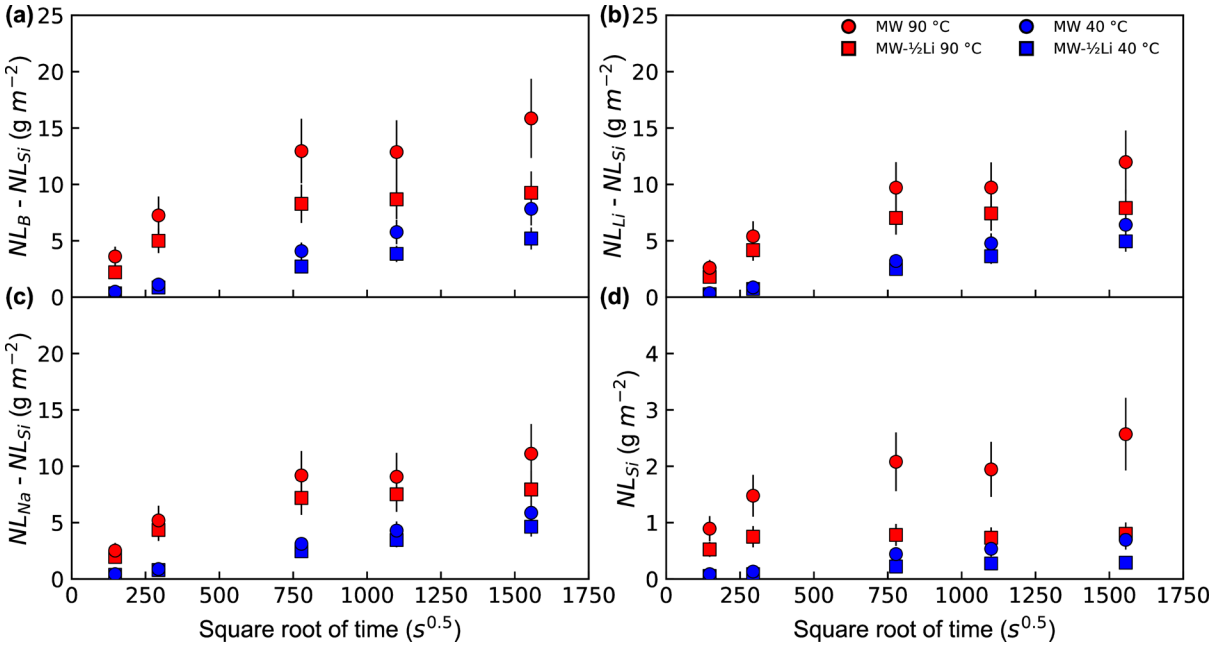

Figure 2: Normalised releases of B (a), Na (b) and Li (c) with the normalized releases of Si subtracted and the normalised releases of Si (d) plotted against the square root of time ($s^{0.5}$). Uncertainties are given to 1 S.D. (Equation 3) and range from 15 to 30% (RSD).

Table 2: Diffusivities of B, Li and Na calculated through linear regressions of the normalised B, Li and Na releases corrected for the normalized Si releases against the square root of time ($s^{0.5}$) (Equation 5). Note that regressions took place for all durations at 40 °C and up to 7 days at 90 °C (linear region). R^2 values associated with these fits are also reported. Values in parentheses represent uncertainties of 1σ propagated from 1 S.E. of the regression coefficient and glass density.

T (°C)	Sample	D_B (m^2 s^{-1})	R^2	D_{Li} (m^2 s^{-1})	R^2	D_{Na} (m^2 s^{-1})	R^2
40	MW	$3.1(6) \times 10^{-18}$	0.9970	$2.0(2) \times 10^{-18}$	0.9970	$1.6(2) \times 10^{-18}$	0.9973
	MW-½Li	$1.4(3) \times 10^{-18}$	0.9985	$1.3(2) \times 10^{-18}$	0.9989	$1.1(1) \times 10^{-18}$	0.9982
90	MW	$2.5(5) \times 10^{-17}$	0.9706	$1.5(4) \times 10^{-17}$	0.9694	$1.3(4) \times 10^{-17}$	0.9662
	MW-½Li	$1.0(2) \times 10^{-17}$	0.9375	$7.7(21) \times 10^{-18}$	0.9411	$7.7(20) \times 10^{-18}$	0.9385

3.2. Machine learning predictions

ML predictions of the base glass NL_i with algorithms trained on the ALTGLASS database showed significant variations in test MSE as a function of feature subset and algorithm chosen. Consistent with previous studies on predicting static glass dissolution using ML methods on unstructured datasets, accurate predictions could not be obtained where more than one 'key' NL_i (B, Li or Na) was absent from the feature subset and the 'complete' feature set (experimental features, leachate pH and all other NL_i) yielded the best predictions [41]. A table of the feature subsets considered in this work and potential additional features to consider in future work is presented in Table S2.

The lowest test MSE and highest R^2 (four responses considered) was attained using a bagged random forest (RF) algorithm across all feature subsets considered. This is attributable to the RF algorithm comprising bootstrap aggregation (bagging), uncorrelated trees arising from considering a random feature subset at each internal node individually, and leaf node number being tuned as a hyperparameter without cost-complexity pruning. In turn, this results in the inability of the RF algorithm to overfit the data through the number aggregated of trees and mitigates against underfitting in many applications, frequently affording accurate predictions of complex feature-response relationships and low test MSE where the number of training observations is sufficiently high [97]. The comparatively poorer metrics of support vector machines and the neural network are consistent with previous observations that these optimisation and search algorithms are highly sensitive to local minima and so cannot accurately predict the highly periodic nature of the glass composition-dissolution behaviour relationship [36]. An in-depth discussion of algorithm performance on the ALTGLASS database and compiled independent unstructured databases as a function of feature subset has been presented previously [39].

Residuals for the best performing algorithm and feature subset showed significant variations as a function of response cation, time and temperature (NL_i predictions as lines in Figure 1); these general trends as a function of NL_i magnitude are also demonstrated in a plot of predicted against measured NL_i (Figure S6). Predicted NL_B were all within uncertainty of the measured values for MW, whilst for MW-½Li 6 hours 40 °C was underestimated and 7 and 14 days 40 °C and 28 days 90 °C were overestimated. Predicted NL_{Na} were generally excellent, but at 6 hours or 1 day were either underestimated or overestimated. Whilst all NL_{Li} predictions were accurate for MW-½Li at 90 °C and both compositions at 40 °C except for MW-½Li at 6 hours (overestimated), the MW 90 °C predictions attained a significantly underestimated, early plateau from 1 day onwards. Similar behaviour was observed for the NL_{Si} predictions for MW at 90 °C from 7 days onwards, which attained an apparent steady state at the correct time but was significantly underestimated. NL_{Si} predictions for 90 °C MW-½Li were accurate but were generally overestimated at 40 °C for both glasses.

These measured-predicted discrepancies likely arose due to some observations in the base glass dataset lying outside the ALTGLASS feature space, which is inhomogeneous: (1) ALTGLASS observations with DI water leachant corresponded to either 90 or 200 °C experiments such that extrapolation to 40 °C was required; (2) leaching time in the database is typically ≥ 7 days (98.37% observations) and is ≥ 10 hours (0.77% observations at 10 hours), such that times < 7 days were not well represented and required extrapolation below 10 hours; and (3) the SiO_2 and B_2O_3 wt.% compositions of MW and MW-½Li were outside the ALTGLASS feature space and Li for MW was poorly represented (95.70% observations were lower).

3.3. Solution pH and activities

Measured pH(25°C) for MW-½Li remained constant with time at 40 and 90 °C (mean: 9.61 ± 0.35 and 9.70 ± 0.35, respectively), whilst pH(25°C) increased for MW up to 7 days at 40 and

90 °C (28 days: 10.30 ± 0.20 and 10.47 ± 0.20, respectively) (Figure 3). Calculated pH(25°C) from measured concentrations showed better agreement with measured values using a $pCO_2 = 0.000$ (Figure 3). Assigning uncertainties of ± 0.20 pH units to the calculated pH(T), the MW and MW-½Li pH(40°C) were constant with time (mean: 9.92 and 9.55, respectively) and pH(90°C) increased up to 1 d (28 days: 9.93 and 9.49, respectively) (Tables S3 and S4).

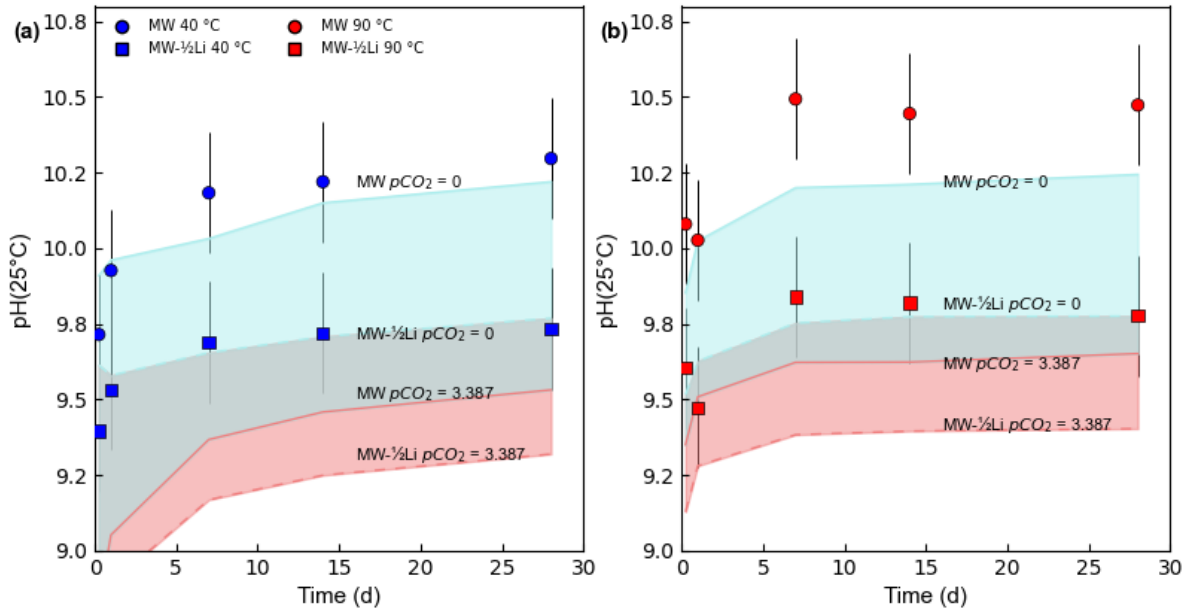

Figure 3: Measured pH(25°C) for the 40 (a) and 90 °C (b) leachates (markers). Uncertainties are reported as ± 0.20 pH units (Section 2.3). The top and bottom edges of each shaded region (labelled) correspond to pH(25°C) for each composition calculated by PHREEQC using the measured leachate concentrations assuming pCO_2 of 0.000 and 3.387, respectively.

The $\ln(r_B)$ showed a near-linear trend with the $a(H_4SiO_4)$ at 40 °C which continued beyond $a^*(H_4SiO_4)$ (saturation with respect to $(SiO_2)_{am}$), whilst the $a(H_4SiO_4)$ at 90 °C varied about the $a^*(H_4SiO_4)$ seemingly independent of the dissolution rate (Figure 4). The latter variations in $a(H_4SiO_4)$ are attributable to small variations in the pH(90°C) with time at values near the pK_a of the reaction $H_4SiO_4 \rightleftharpoons H_3SiO_4^- + H^+$ (9.17 at 90 °C [98]).

Taking the deviations from the first-order rate law as characteristic times for the start of residual rate regime, t_r, yielded values of 7 days at 40 °C and < 6 hours (no clear inflection observed) at 90 °C. These values are significantly shorter than the t_r of 180 days reported for Li and B-bearing basaltic glasses (30 and 90 °C, DI water, S/V of 10^5 m^{-1}) [82] and 200 to 450 days for

441 glasses ranging in complexity from Na-Al borosilicates to a full-scale simulant HLW glass
442 (SON68) (90 °C, DI water, S/V of 8000 m^{-1}) [16]. However, the t_r for ternary Na borosilicates
443 has also been previously reported as < 1 day (90 °C, DI water, S/V of 8000 m^{-1} [17].

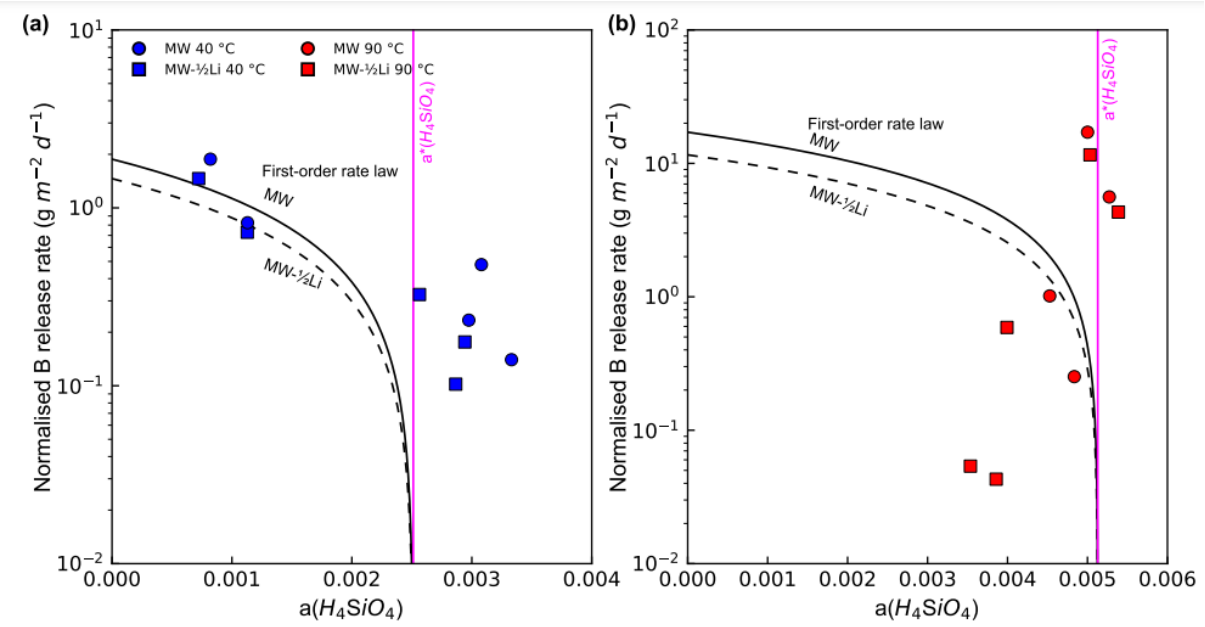

444

445 *Figure 4: Normalised B release rates (log scale) against $a(H_4SiO_4)$ for the 40 °C (a) and 90 °C (b) solution concentrations.*
446 *Black lines show first-order rate laws (Equation 6) with magenta lines denoting $a^*(H_4SiO_4)$ with respect to $(SiO_2)_{am}$.*

447

448 ## 3.4. Imaging and compositional analyses of the glass surfaces

449 SE images of the leached particles revealed small precipitate clusters after 28 days at 40 °C,
450 whilst at 90 °C secondary phases formed in sparse patches and near-uniform layers across the
451 particle surfaces for MW-½Li and MW, respectively (Figure 5).

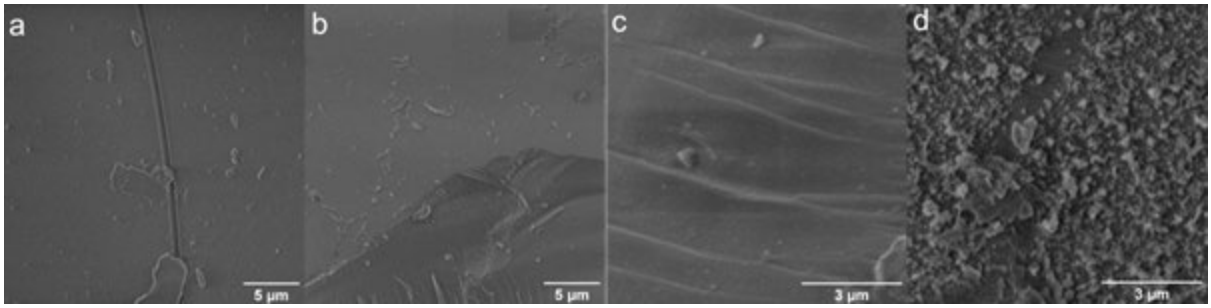

Figure 5: SE images of leached powder surfaces. MW-½Li leached for 28 days at 40 (a) and 90 °C (b) and MW leached for 28 days at 40 (c) and 90°C (d).

EDS revealed four phases were present for both samples leached at 90 °C: (1) a smooth surface rich in Si, (2) surfaces covered in secondary phases rich in Na relative to (1), and clusters of (3) Na-rich and (4) Si-rich precipitates (Figure 6). Consistent with less significant surface alteration at lower temperatures, only Si-rich and Na-rich surface features and no precipitate clusters of sufficient size for analysis were observed at 40 °C (Figure S7). The measured Si/Na and Si/O ratios of these phases are presented in Table 3.

The Si-rich surface composition was consistent with either the preferential leaching of Na or complete dissolution-precipitation to leave a Si-rich altered surface, whilst the Na-rich surface layer was consistent with the precipitation of Na-bearing secondary phases. Whilst the Si/Na ratio of the Na-rich precipitate was in broad agreement with that of magadiite for MW ($NaSi_7O_{13}(OH)_3 \bullet H_2O$), for MW-½Li it better corresponded to natrosilite ($Na_2Si_2O_5$). Differences in the Si/Na ratios of the precipitate-covered surfaces between MW and MW-½Li are attributable to the higher Li contents of the former alongside the comparatively smaller precipitates for MW-½Li likely resulting in a larger fraction of the interaction volume representing the underlying altered or pristine glass. This view is consistent with the leached Si-rich surfaces free from secondary phases having Si/Na ratios being within uncertainty for MW and MW-½Li.

Table 3: Elemental molar ratios for the nominal pristine compositions and the mean EDS measurements for the 28 day 40 and 90 °C leached samples. Uncertainties correspond to 1 S.D. propagated from individual values. Note that the Si-rich and Na-rich surfaces were averaged across 40 and 90 °C, whilst the Na-rich and Si-rich phases were only observed at 90 °C.

	MW		MW-½Li	
Phase	**Si/Na**	**Si/O**	**Si/Na**	**Si/O**
Pristine (nominal)	2.9	0.3	2.9	0.3
Si-rich surface	14.2 ± 3.1	0.5 ± 0.1	12.6 ± 1.7	0.5 ± 0.1
Na-rich surface	6.5 ± 1.3	0.5 ± 0.1	3.4 ± 0.6	0.5 ± 0.1
Na-rich phase	7.8 ± 1.7	0.5 ± 0.2	1.2 ± 0.3	0.4 ± 0.2
Si-rich phase	10.1 ± 1.3	0.5 ± 0.1	5.4 ± 0.9	0.5 ± 0.1

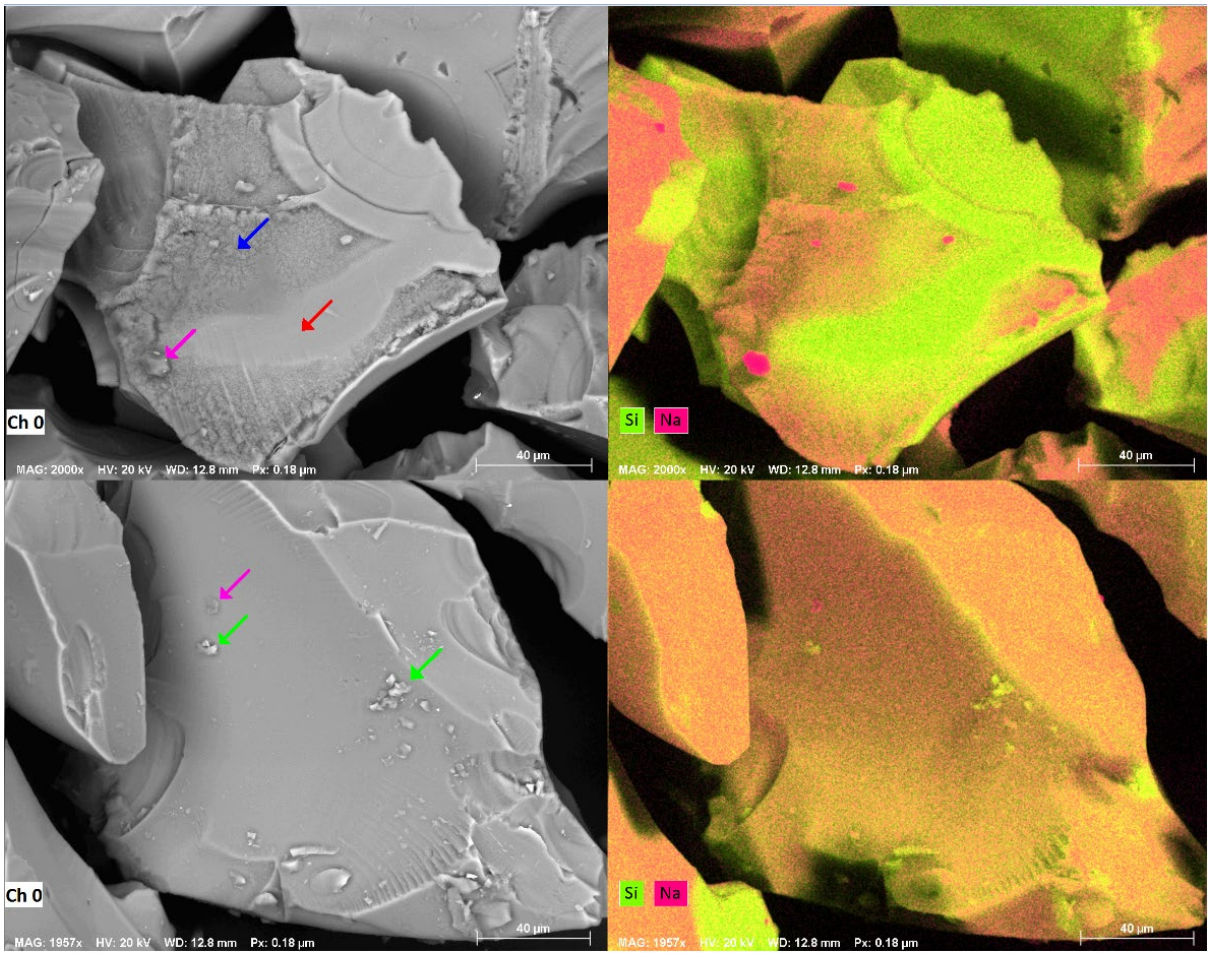

Figure 6: BSE images (left) and EDS compositional maps (right) of Si (yellow) and Na (magenta) for the MW-½Li 90 °C 28 day sample. Arrows in the BSE images correspond to the Si-rich surface (red), Na-rich surface (blue), Na-rich precipitates (magenta) and Si-rich precipitates (green).

Pristine MW has been previously studied by Raman spectroscopy [99]. The Raman spectra of pristine and leached MW and MW-½Li are presented in Figure 7. Notably, two surface morphologies were visible by optical microscopy for MW at 90 °C: a 'smooth' featureless surface with a spectrum resembling the pristine glass and a 'rough' highly altered surface.

For MW at 40 °C and 'rough' MW and MW-½Li at 90 °C, there was a slight reduction in the band at approximately 640 cm^{-1} and a significant decrease in the band at approximately 1450 cm^{-1}. The former is attributable to metaborate rings [100], ^{IV}B units in danburite-like units [101] or a combination of both [102], whilst the latter is attributable to boroxol rings and B-O^- bonds [91,100]. The small broad band at 805 cm^{-1} decreased but a larger band formed at 795 cm^{-1}. The former is attributable to ^{IV}B units [100,101] from borate rings with up to two ^{IV}B units [103–105], whilst the latter represents Si-O-Si bond bending vibrations in amorphous silica [106–108].

The band at approximately 510 to 530 cm^{-1} shifted to 450 to 480 cm^{-1}, and represents the partial deformation and stretching of Si-O-Si bonds [100]. This shift is attributable to increased Q^n or a decrease in reedmergnerite unit concentration [87]. Similarly, there is a significant decrease in intensity for the band from 900 to 1250 cm^{-1}, which represents Q^n [54,87,100,109]. The significant loss of intensity rendered a quantitative assessment of the change in Q^n following dissolution impossible. However, previous ^{29}Si NMR experiments on ISG and simplified borosilicate glasses leached under SiO_2 saturated conditions showed no significant change in Q^n in the gel layer [110,111]. Bands at 1630 cm^{-1} represent free and silanol group H-bonded water bending modes [107].

For 'rough' MW a sharp band appeared at 1090 cm^{-1}. Comparisons of sodium silicate glasses and crystallised glasses (post-thermal treatment) have previously attributed a similarly sharp peak at 1080 cm^{-1} to $Na_2Si_2O_5$ [103] or to the Na silicate hydrate magadiite [112]. The absence of other peaks associated with this phase reflects either its small quantity or poorly crystalline nature. For MW at 40 °C a broad band appeared at approximately 1350 cm^{-1}, which is attributable to B-O-B asymmetric bond stretching for non-ring 'free' ^{III}B units [102,108]. This is consistent with the transformation of ^{IV}B to ^{III}B units prior to solvation resulting in a localised increase in the f(^{III}B), which was previously postulated to occur near the gel-solution interface

[113]. The absence of this band at 90 °C is due to either an insufficient concentration of ^{III}B or a slower ^{IV}B to ^{III}B unit transformation rate relative to the ^{III}B hydrolysis rate at higher temperatures. The Raman spectrum for MW-½Li at 40 °C was intermediate between that of the pristine glass and MW-½Li at 90 °C with bands at 1350 and 1630 cm^{-1}. Notably, the band at 1630 cm^{-1} had a higher relative intensity than in the other spectra.

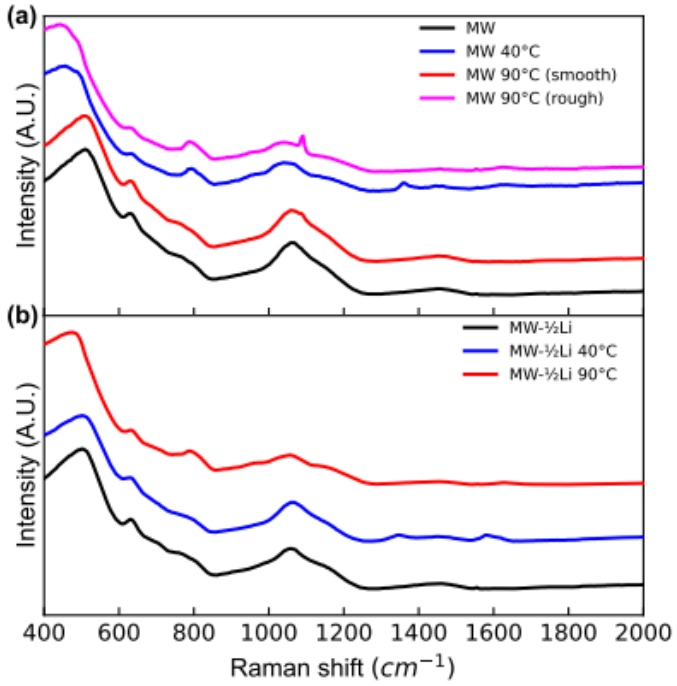

Figure 7: Raman spectra for the pristine and leached MW (a) and MW-½Li (b) glasses. Spectra were normalised to the intensity of the peak at 450 to 520 cm^{-1} and stacked for clarity.

3.5. Identification and quantification of secondary phases

XRD revealed no significant changes following dissolution (Figure S5), consistent with the Na-rich secondary phases forming with insufficient mass or crystallinity for detection.

PHREEQC calculated saturation indices (Tables S3 and S4, and Figure S8) demonstrated that all leachates were supersaturated with respect to chalcedony, cristobalite (except 40 °C 6 hours) and quartz and were near equilibrium with respect to amorphous silica (except 40 °C 6 and 12 hours). The MW leachates from 1 day at 90 °C and 28 days at 40 °C were supersaturated and near equilibrium with respect to di-Li silicate, respectively. Whilst magadiite was

supersaturated or near saturation in all but the MW-½Li 40 °C 6 hour leachates, its entry in the database comprised solely a log(K) value. Note that all solutions were undersaturated with respect to all Na silicates in the database (natrosilite, Na_2SiO_3, Na_4SiO_4 and $Na_6Si_2O_3$).

^{23}Na MAS-NMR spectra showed that Na was present in an additional environment following dissolution at -5.7 ± 1.1 ppm (Figure 8). A larger fraction of Na in this environment was estimated for MW at 40 °C than MW-½Li at 90 °C despite the latter having a larger estimated fraction of glass altered (Section 3.1). To a first order, the mass of Na in this phase was approximated through quantifying its relative area (Table 4). The chemical shift of this ^{23}Na MAS-NMR peak is consistent with literature observations for an AFCI glass (a 28-component simulant waste glass) leached for 1 month in DI water at 90 °C, with ^{23}Na -^{1}H CP-MAS NMR on this sample demonstrating Na retained in the altered layer produced a chemical shift indistinguishable from the pristine glass [114]. Notably, all leachates were undersaturated with respect to Na silicates. Further, the chemical shift falls within the range reported for Na metasilicate hydrates (-7.2 to 2.3 ppm) [115], broadly agrees with values reported for magadiite, kenyaite and octosilicate (-4.8 to -1.7 ppm) [116,117], and does not agree with reported values for crystalline Na metasilicates and disilicates (8.3 to 22.8 ppm experimental, 7.6 to 24.1 ppm calculated) [115,118–120]. It was concluded this peak corresponded to a poorly crystalline Na silicate hydrate secondary phase (Figure 6).

Water adsorption on the pristine glass was not measurable by static ^{6}Li-^{1}H CP-NMR experiments. At 90 °C 28 days, no signal was observed for MW-½Li, whilst a small peak was observed for MW (Figure 8). This is consistent with the PHREEQC calculations in showing that the 90 °C 28 day MW-½Li and MW solutions were undersaturated and supersaturated with respect to a di-Li silicate phase, respectively.

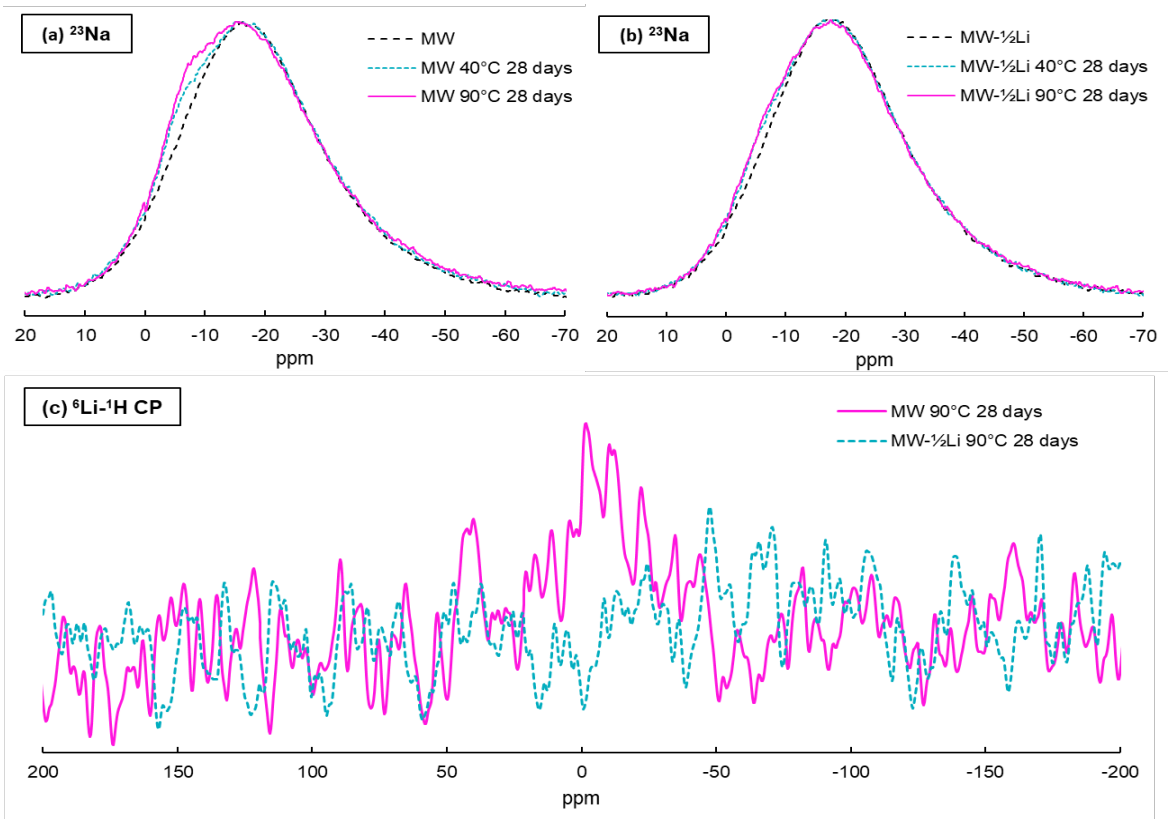

Figure 8: ^{23}Na MAS-NMR experiments for pristine and 28 day 40 and 90 °C leached MW (a) and MW-½Li (b), and static ^{6}Li-^{1}H CP-NMR experiments for 28 day 90 °C leached MW and MW-½Li (c). Note that ^{23}Na MAS-NMR spectra were normalised to their respective maximum pristine glass peak heights to afford a direct comparison, whilst the ^{6}Li-^{1}H CP-NMR spectra were normalised to the mass of sample analysed and number of scans acquired.

Table 4: Quantification of the area of the ^{23}Na MAS-NMR peak formed following dissolution (Figure 8) relative to the total area analysed (%), the estimated mass of Na in this phase (mg of phase per g of sample), and quantification of the fraction of ^{III}B in the sample relative to ^{IV}B (f^{III}B) before and after dissolution. Uncertainties reported for the Na quantifications are given to 1σ arising from the fitting procedure and are propagated to include dissolution experiment uncertainties. Uncertainties for the B quantifications assumed a conservative 5% uncertainty associated with the quantified area of each peak.

	MW			MWH		
	Pristine	**40 °C 28 d**	**90 °C 28 d**	**Pristine**	**40 °C 28 d**	**90 °C 28 d**
New Na peak (%)	-	2.00 ± 0.05	3.28 ± 0.07	-	0.50 ± 0.03	0.66 ± 0.03
[Na] peak (mg g^{-1})	-	1.4 ± 0.4	2.6 ± 0.7	-	0.4 ± 0.1	0.5 ± 0.1
f(^{III}B)	0.342 ± 0.014	0.352± 0.015	0.305± 0.013	0.353± 0.015	0.337± 0.014	0.329 ± 0.014
^{III}B/^{IV}B	0.519± 0.024	0.543± 0.029	0.439± 0.025	0.546± 0.023	0.509± 0.025	0.490 ± 0.025

3.6. Altered layer structures

The pristine structures of Li-Na (equimolar) borosilicates as a function of composition have been previously reported in detail elsewhere [48]. Here, the ^{11}B MAS-NMR spectra showed

apparent narrowing of the ^{IV}B peak and a decrease in the ^{III}B peak intensity at -4.5 and 7.5 ppm, respectively, following dissolution (Figure 9). Quantification showed that no significant change in the fraction of ^{III}B units, f(^{III}B), followed dissolution at 40 °C whilst a slight decrease in the f(^{III}B) was observed at 90 °C for both compositions (Table 4). This decrease is consistent with previous ^{11}B MAS-NMR experiments on seven-component borosilicate glasses [20], and is attributable to the weaker bonding of ^{III}B units to the glass network than ^{IV}B units leading to a higher fraction of ^{IV}B units being temporarily retained in the gel layer [113]. This decrease in f(^{III}B) is associated with the preferential hydrolysis of rings, which tend to aggregate, over ^{IV}B units [16,91], with the ring to non-ring ^{III}B ratio decreasing following dissolution at 90 °C from 4.80 ± 0.07 to 4.26 ± 0.05 for MW and from 5.44 ± 0.08 to 4.51 ± 0.06 for MW-½Li.

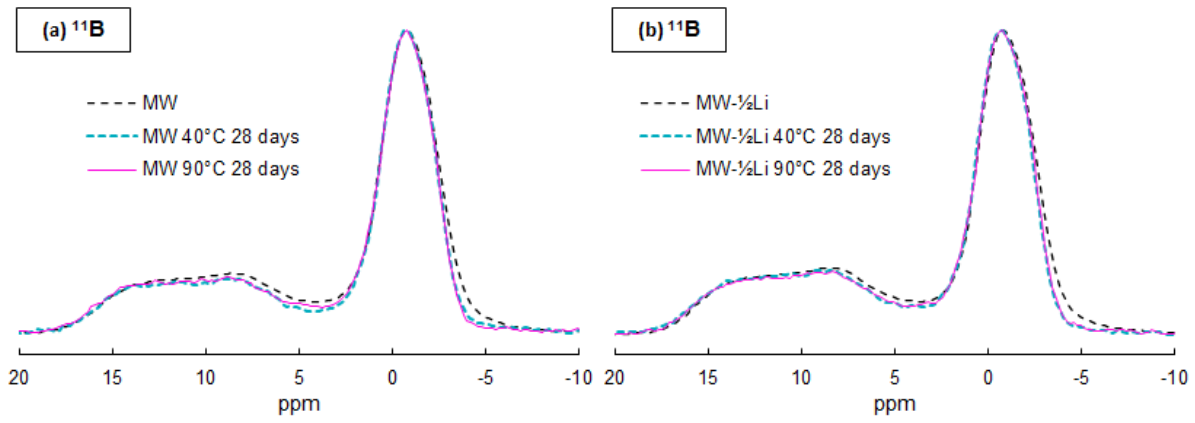

Figure 9: ^{11}B MAS-NMR experiments for pristine and 28 day leached MW (a) and MW-½Li (b). Spectra were normalised to their respective maximum BO_4 peak heights (-0.8 ppm) to afford a direct comparison between samples.

SEM-EDS of the polished resin-mounted pristine MW and MW-½Li powders showed no alteration occurred during resin mounting and polishing (Figure S9). At 40 °C, well-defined altered layers depleted in Na were visible for both MW and MW-½Li (Figure 10). Altered layer structures for the 90 °C samples were more complex (Figure 11): MW-½Li particles now contained large regions of alteration (Na depletion), with some particles comprising Si-rich layers covering Na-bearing cores which contained voids. Similar features were observed for MW at 90 °C, but with many of these Si-rich layers being detached from each other and some

584 particles exhibiting significant apparent internal alteration alongside secondary phase
585 precipitation.

586 Quantification of these EDS maps (Table S5) confirmed these observations, showing that at
587 40 °C the main particle phase was unaltered whilst the alteration layer had lost 51 to 58% of
588 its initial Na contents. At 90 °C, the Si-rich layers were nearly entirely depleted in Na, whilst
589 the inside surfaces of the innermost layers (where multiple were observed) were partially
590 enriched in Na relative to outer layer. Maps of particles where these layers were well separated
591 show that this is attributable to the internal precipitation of Na-bearing secondary phases. The
592 Na-bearing cores in the MW and MW-½Li particles were slightly depleted in Na and within
593 error of the measured pristine composition, respectively. Where inner precipitates were
594 observed in the 90 °C MW sample these were enriched in Na relative to their surroundings,
595 with the Si/Na ratios with uncertainty of those at the surface (12.3 ± 3.5 and 7.8 ± 1.5,
596 respectively). These results suggest the layered Si-rich layer-core structures act as an
597 intermediate step between an alteration layer forming and significant internal alteration.

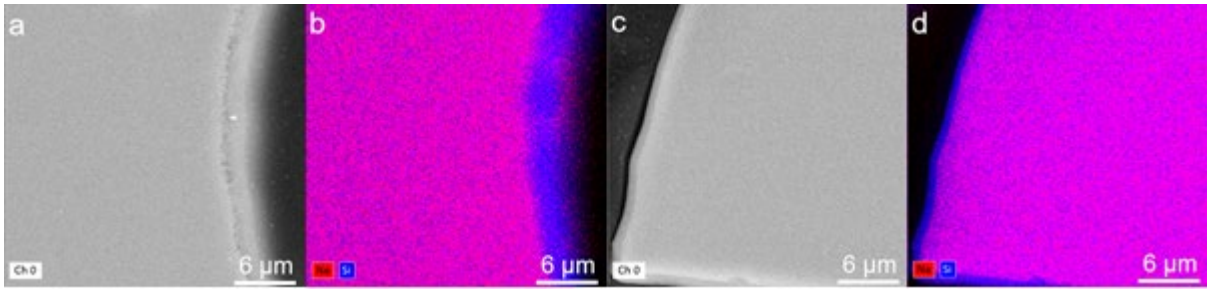

598
599 *Figure 10: BSE images (a and c) and EDS Na (red) and Si (blue) maps (b and d) for MW (a and b) and MW-½Li (c and d)*
600 *leached for 28 days at 40 °C.*

601

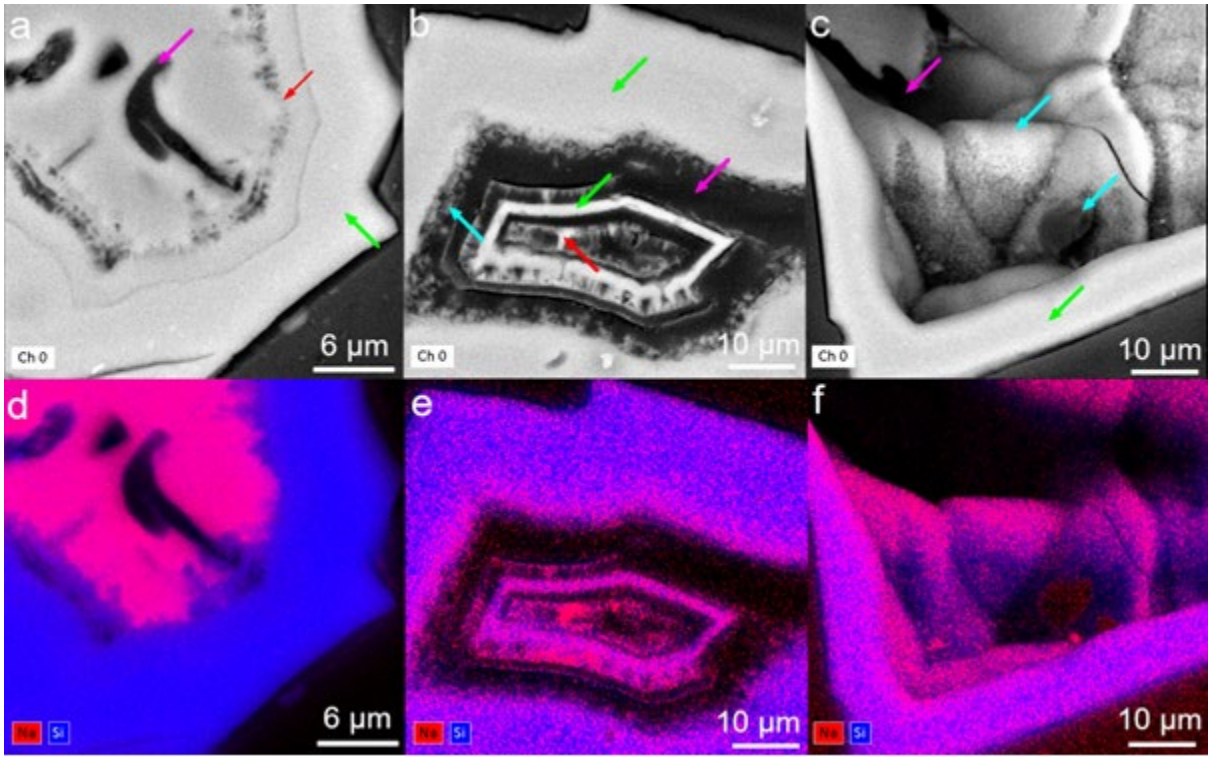

Figure 11: BSE images (a, b and c) and EDS Na (red) and Si (blue) maps (d, e and f) for the resin-mounted particles of 28-day 90 °C leached MW-½Li (a and d) and MW (b, c, e and f). Arrows denote voids (magenta), the Na-bearing cores (red), Si-rich layers ('shells') (green) and Na-rich secondary phases (cyan).

Where an altered layer was evident (40 °C) or a near-unaltered core was present (90 °C), altered layer thicknesses for the 28-day leached samples were estimated using ImageJ software (NIH) through thresholding the Na-Si EDS maps. Thicknesses of 3.9 ± 0.9 and 30.4 ± 5.9 µm were estimated for MW at 40 and 90 °C, respectively, and 0.8 ± 0.2 and 8.7 ± 0.8 µm for MW-½Li at 40 and 90 °C, respectively. Notably, these values for 90 °C, 40 °C MW and 40 °C MW-½Li are significantly higher, within uncertainty and significantly lower, respectively, than the thicknesses estimated from the leachate B concentrations using a shrinking core model. This is in part attributable to dissolution proceeding in a non-uniform manner, as evidenced by observed variations in altered layer thicknesses even within a given particle.

4. Discussion

4.1. Insights from machine learning predictions

Excluding the significantly underestimated predicted long-term releases (Li and Si from MW at 90 °C), the predicted NL_i were generally excellent: 65.0% and 93.9% were within 25% of their measured values and all predictions were within 66.0% and 34.0% at 40 and 90 °C, respectively. The accurate predictions for NL_B and NL_{Na} are consistent with previous observations that NL_{Na} is a strong feature for learning NL_B in the ALTGLASS database [39]. The comparatively poorer predictions at 40 °C are attributable to the ALTGLASS feature space requiring extrapolation for this lower temperature, suggesting either (1) poor correlation between the temperature dependence of dissolution for complex glasses in ALTGLASS from 90 to 200 °C and the base glasses from 40 to 90 °C, or (2) differences in the rate of change of feature importance weights or predictive strength as a function of temperature in these two temperature ranges.

Excluding NL_{Li} and NL_{Si} for MW at 90 °C, the prediction residuals were not systematic. These were attributable to uncertainties associated with the ALTGLASS feature space often requiring extrapolation (absence of data: <90 °C, similar B_2O_3 and SiO_2 wt.%, and <10 hours) or being heterogeneous (lack of data: < 7 days and similar Li_2O wt.% to MW), thereby destabilising the accuracy of these predictions. However, it should be noted that first order analysis revealed no clear correlation between predictions and measurements being within propagated uncertainty and these feature space factors; the predictability of a response for an observation outside the training feature space is also influenced, in part, by the algorithm used and the monotonicity of the feature-response relationship [38]. Further, given the large number of experimental features, the diversity of reported literature observations for these features and the long

timescales required for data acquisition associated with glass dissolution experiments, the curse of dimensionality is significant when predicting glass dissolution behaviour.

Predicted NL_{Li} and NL_{Si} for MW at 90 °C reached a significantly underestimated constant value and apparent steady state, respectively, with Li predicted to reach this early (1 instead of 7 days). The excellent NL_B predictions for all experiments, NL_{Li} predictions for MW at 40 °C and NL_{Si} for MW-½Li at 90 °C all demonstrate this is not solely attributable to the MW Li_2O and SiO_2 wt.% being largely outside the ALTGLASS feature space. All measured leachate concentrations and their ratios were well within this feature space (see also Section 2.5). Notably, the excellent predicted NL_{Si} for MW-½Li at 90 °C and comparatively poorer predictions for all other experiments coincide with an apparent steady state Si concentration being reached before 6 hours for the former and after 7 days for the latter. Further, the predicted NL_{Li} at 90 °C for MW-½Li are higher than MW at 7 and 14 days before converging to similar values at 28 days (7.72 and 7.59 g m^{-2}, respectively), despite the higher measured pH, other NL_i and Li_2O wt.% for MW and identical initial experimental conditions. This shows that these features in isolation are not responsible for these anomalous predictions.

Whilst four NL_i were predicted as responses, all reported oxide wt.% species of the complex glasses from the ALTGLASS database were used as features, excluding those removed during feature selection. In turn, whilst Li_2O, B_2O_3, Na_2O and SiO_2 wt.% features for the base glasses were non-zero, all other oxide wt.% elements were set to zero (complete list of oxides considered in Table S2). It is postulated that these compositional features or combinations thereof limited the predicted NL_{Li} and NL_{Si}. For example, all observations in the ALTGLASS database with >200 μg mL^{-1} Li at 28 days, 90 °C and 2.0 ± 0.2 m^2 L^{-1} were Mg-bearing. The absence of these species from the base glass compositions in effect creates a pseudo-limit where ALTGLASS-trained algorithms are unable predict higher NL_i unless these additional compositional species are present, which appears only slightly influenced by the NL_i features.

663 The higher predicted NL_{Si} limit for MW at 90 °C shows that the differences in observations
664 between MW and MW-½Li, such as the non-response NL_i values, exerted a greater influence
665 on the predicted 90°C NL_{Si} than the NL_{Li}.

666 These poorer NL_{Li} and NL_{Si} predictions may be interpreted as reflecting greater similarities in
667 the dissolution behaviour of MW-½Li and the complex ALTGLASS glasses at 90 °C than for
668 MW, and hence differences in the dissolution behaviour of MW and MW-½Li at 90 °C.
669 However, it should be noted that ML predictions for a given algorithm depend on the training
670 dataset, including the optimal hyperparameters selected by cross-validation, and its relation to
671 the test data. In turn, heterogeneity or extrapolation of the ALTGLASS feature space for some
672 experimental features herein prevent correlating these differences in predictions with
673 differences in mechanisms. Whilst ML presents a useful tool for identifying glasses with
674 similar or anomalous predictions (clustering), there is insufficient evidence here to correlate
675 such predictions with similarities in dissolution mechanisms between glasses.

676 Overall, the bagged random forest algorithm predictions for NL_B and NL_{Na} were accurate,
677 capturing the significant differences in dissolution behaviour between MW and MW-½Li
678 despite these glasses comprising identical elemental species. This demonstrates potential for
679 the use of compiled structured datasets in predicting NL_i in small-scale glass dissolution
680 laboratory experiments, without needing to explicitly assume the mechanisms underpinning
681 dissolution. However, the comparatively poorer overall predictions for NL_{Li} and NL_{Si} highlight
682 the importance of underpinning these methods with an extensive, diverse and homogeneous
683 training dataset. The poor predictability observed when using feature subsets lacking other NL_i
684 suggests that the standalone ML methods applied herein may be complementary to dissolution
685 experiments wherein only limited data are acquired, such as during the continuous monitoring
686 of leachate pH and B concentrations through in-situ Raman spectroscopy [121,122].
687 Ultimately, these results have shown that further improvements, likely both in the methods

(beyond standalone models [36]) and the datasets used, are required to predict dissolution behaviour from experimental features. Future datasets could also include additional features, such as physics-informed features, to improve prediction accuracy for some species (see Table S2). For example, a cationic strength feature could assist in further distinguishing between the effects of Li and Na, with the Li/Na ratio having been shown to significantly influence dissolution behaviour in certain systems [20,44,93]. This has significant implications for predicting behaviour for relatively less studied dissolution conditions, such as highly alkaline environments [123], and phenomena, such as resumption (stage III) [124–127]. It is anticipated cluster analysis (unsupervised learning) will be a valuable next step: cluster analysis groups glass compositions and experimental conditions to provide a data-driven perspective on how these features affect dissolution behaviour and which are crucially important.

4.2. Changes in dissolution behaviour with Li content and temperature

Two competing pristine structure effects caused differences in the dissolution kinetics of MW relative to MW-½Li. First, the higher total alkali concentration of MW enhances dissolution through lowering Q^n, in turn also relaxing steric constraints associated with activated complex formation during hydrolysis [128]. This is also consistent with percolation theory, where alkalis form nanoscale clusters with localised alkali-alkali order which interconnect above a threshold concentration to yield rapid ion transport [129–131]. The faster rupture of alkali and B-bearing bonds relative to Si-O-Si facilities faster glass hydration and exposes a greater effective surface area of the Si network for hydrolysis [95,132,133].

Second, the cationic field strengths of Li and Na causes differences in their short and medium range order [129]: Li preferentially forms Si network Li-NBO bonds over charge compensating $[BO_4]^-$ [48,90]. Deviating from an equimolar Li/Na ratio has been shown to be detrimental to aqueous durability [20,93], likely due to the different ionic radii of Li and Na inhibiting

transport along shared percolation pathways [134]. Similarly, a B/Na ratio of 1.0 optimises aqueous durability in Na borosilicates [95]; the [total alkali]/B ratios are 1.14 and 0.56 for MW and MW-½Li, respectively. As such, the higher total alkali concentration effects are likely partially offset by the equimolar Li/Na ratio and near-unity [total alkali]/B ratio of MW. The normalised B releases being within uncertainty for MW and MW-½Li up to 7 days at 40 °C is attributable to a slower rate of hydrolysis at lower temperatures weakening the Q^n effect [135].

The calculated pH(40,90°C) being higher and the measured pH(25°C) increasing up to 7 days for MW facilities more extensive hydrolysis due to a higher Si concentration being required to reach a steady-state in solution [98,136]. The higher Si concentrations for MW at both temperatures are therefore attributable to the Q^n effect and higher leachate pH.

The higher leachate concentrations for MW resulted in higher rates of Na silicate hydrate precipitation and the precipitation of di-Li silicate at 90 °C and likely at 40 °C. A higher degree of alteration and larger estimated relative masses of Na silicate hydrate secondary phases were observed for MW but normalised Na releases were within uncertainty for MW and MW-½Li up to 28 days at 90 °C. This suggests the precipitation of di-Li silicate raises affinity for hydrolysis, resulting in further Si release which then precipitates as both phases to increase the mass of Na incorporated into secondary phases. In consuming Si, both precipitates drive affinity for gel or glass dissolution to inhibit condensation reactions and the formation of a passivating gel. At 40 and 90 °C the ratio of Na in secondary phases for MW and MW-½Li estimated by NMR are within uncertainty, consistent with the same effect occurring at 40 °C.

The SEM-EDS maps, geochemical modelling and Raman spectra were consistent with a gel layer formed of amorphous silica $(SiO_2)_{am}$ at 28 days. Dissolution beyond and around saturation with respect to $(SiO_2)_{am}$ at 40 and 90 °C, respectively, is consistent with the higher solubility of ternary Na borosilicates than $(SiO_2)_{am}$ [137], in contrast with more complex compositions,

736 such as ISG and B-doped basaltic glass [138,139]. In turn, delimiting the residual rate using
737 the solubility of $(SiO_2)_{am}$ likely underestimated the true transition times for MW and MW-½Li.

738 Notably, 'free' water was present in the leached sample Raman spectra, with a higher relative
739 intensity for MW-½Li at 40 °C than at 90 °C or MW at 40 and 90 °C. This shows that gel
740 porosity for MW-½Li at 90 °C and MW was sufficiently large for significant water
741 concentrations to be removed during drying, whilst that at 40 °C for MW-½Li retained more
742 water. This may be attributed to the gel layer forming faster at 90 °C and for MW, providing
743 more time for the porosity of the gel at the surface to age than MW-½Li at 40 °C [95,133].
744 Similarly, the MW gel layer appeared significantly thicker but less passivating. This result at
745 90 °C is consistent with previous deuterated water tracer experiments on Na borosilicates
746 (90 °C, 0.5 M $NaHCO_3$) which showed that the gel layer at 142 hours presented an ineffective
747 barrier against the transport of water species [140].

748 The observed $t^{-0.5}$ rate dependence for the normalised Li, B and Na releases corrected for Si at
749 40 °C and up to 7 days at 90 °C are consistent with diffusive processes contributing to the
750 normalised releases, with higher apparent diffusivities for MW due to its pristine structure, as
751 described by percolation theory, presenting a weaker barrier to hydration. Notably, the 6 and
752 12 hour leachates at 40 °C were undersaturated with respect to $(SiO_2)_{am}$. As such, it is
753 postulated diffusion occurred during the hydration of the pristine glass, ion-exchange or B
754 hydrolysis, and the subsequent outward transport of glass species (interdiffusion), rather than
755 diffusion across the gel layer. Literature SEM, TEM and ToF-SIMS observations showed that
756 gel initially formed on a Na borosilicate (90 °C, pH(90°C) 9.0, S/V 3000 m^{-1}) as a precipitate
757 through an interface-coupled dissolution precipitation (ICDP) mechanism (complete
758 dissolution through interfacial water spatially and temporally coupled to precipitation), which
759 then transitioned to an incomplete hydrolysis coupled with in-situ reorganisation (condensation
760 and precipitation) mechanism once the gel matured to become sufficiently transport-limiting

761 [79]. In this view, it is postulated diffusion occurred in a narrow width ahead of the Si network
762 hydrolysis front, with hydrolysis being complete and the gel constituting precipitated $(SiO_2)_{am}$.
763 However, the results reported herein cannot be used to trace the mechanisms of gel formation
764 and the presence of a mechanistic transition to incomplete hydrolysis cannot be confirmed.

765 Deviation from $t^{-0.5}$ rate dependence at 90 °C shows that diffusive processes did not
766 significantly contribute to the normalised releases beyond 7 days. Observations of gaps
767 between $(SiO_2)_{am}$ layers and voids in the 'cores' at 28 days 90 °C by SEM-EDS are consistent
768 with in-situ Raman studies on Na borosilicates (90 °C 0.5 M $NaHCO_3$ and 70 °C 0.1 M HCl)
769 which showed that such regions are water-rich, corresponding in some instances to the
770 interfacial water described by the ICDP model [107,140]. As such, it is postulated that beyond
771 7 days at 90 °C dissolution is controlled by complete network hydrolysis coupled to
772 precipitation in the absence of significant interdiffusion. The lower relative significance of
773 interdiffusion would be favoured earlier at higher temperatures due to the higher activation
774 energy of hydrolysis [135], and may also be affected by the evolution of gel porosity with time.
775 The $t^{-0.5}$ rate dependence and observation of $(SiO_2)_{am}$ at the surface for both temperatures by
776 Raman (weak band for MW-½Li at 40 °C) suggested similarities in the dissolution mechanisms
777 at both temperatures before 7 days. However, the timescales probed herein appear insufficient
778 to confirm the presence of interfacial voids at 40 °C.

779 SEM-EDS of the Si-rich layers formed at 90 °C showed that (1) where two layers formed the
780 inner had a higher Na/Si ratio than the outer and (2) these layers had a significantly higher
781 Na/Si for MW than MW-½Li. This suggests that Na silicate hydrates precipitated within these
782 layers, with a concentration gradient from the core to the surface resulting in more precipitation
783 in the inner layers than the outer layers. This is supported by the significant amounts of
784 precipitates observed on the inner surfaces of the outer layers and the outer surfaces of the inner
785 layers. The more significant precipitation in these layers for MW is consistent with its larger

786 mass of Na silicate hydrate phase estimated by NMR, facilitated by its higher Si concentration
787 in solution and pH. It is postulated the precipitation of these secondary phases partially blocked
788 porosity, thereby contributing to the passivating properties of these $(SiO_2)_{am}$ layers and the
789 slowing of the dissolution rate. However, it cannot be determined if precipitation within the
790 $(SiO_2)_{am}$ layers occurred during dissolution, drying or both.

791 Note that the effects outlined above are highly coupled and represent a feedback mechanism
792 for the enhanced dissolution kinetics of MW. Ultimately, the simplistic base glass dissolution
793 behaviour presented here contributes to our understanding of how simultaneous variations in
794 total alkali contents and Li/Na ratios could impact complex HLW glass aqueous durability.
795 However, other effects, such as intermediate network formers, phase separation and secondary
796 phases assemblages also require consideration. It is also notable that the addition of 25 wt.%
797 simulant Magnox HLW to MW significantly improves aqueous durability [141].

5. Conclusions

Accurate ML predictions of the NL_B and NL_{Na} were achieved for the base glasses where the feature subset included pH and at least one NL_i. Extrapolating the high temperature, long duration feature space defined by complex glass dissolution experiments (ALTGLASS) to 40 °C and short times yielded poorer predictions for MW and MW-½Li for some species. However, experimental features outside the training set feature space were shown to not be a requirement for poor predictive performance. The absence of common HLW glass species from the composition of MW, which is itself largely outside the ALTGLASS compositional feature space, resulted in poor predictions of the long-term NL_{Li} and NL_{Si} at 90 °C. Overall, these results highlight the importance of a homogeneous, broad training dataset which covers the compositions and conditions of interest, and highlights potential applications for standalone ML algorithms in complementing continually acquired, in-situ datasets.

The faster dissolution kinetics of MW than MW-½Li were consistent with the coupled processes of pristine network depolymerisation, poorly crystalline Na silicate hydrate and di-Li silicate precipitation, and passivating $(SiO_2)_{am}$ gel layer formation inhibition being enhanced for MW. The MW-½Li gel at 40 °C trapped water species more readily during drying, as was consistent with a finer porosity than at 90 °C and MW at both temperatures. Further, the gel formed on MW was observed to be thicker than that formed on MW-½Li, but kinetics suggested it was less passivating at any given time. This is consistent with faster dissolution kinetics producing a larger, more open gel structure with more time for its porosity to mature. BO_3 ring structures were shown to leach preferentially at 90 °C, likely due to their tendency to aggregate. However, significant concentrations of BO_3 observed at the 40 °C surface were consistent with $[BO_4]^-$ transforming prior to dissolution. Diffusive processes were significant at both temperatures, with a slowing rate and evolving gel porosity causing diffusion to become irrelevant at longer times at 90 °C. This result alongside observations of voids in the altered

823 layer structures at long times at 90 °C were most consistent with a transition from interdiffusion
824 coupled with slower complete hydrolysis and precipitation to an ICDP model with time.

825 **Acknowledgements**

826 The authors would like to thank G. Lampronti (Earth Sciences, University of Cambridge) for
827 training and assistance throughout the XRD and SEM analyses, I. Buisman (Earth Sciences,
828 University of Cambridge) for training and assistance throughout the EPMA and SEM analyses,
829 and R. Guo (Earth Sciences, University of Cambridge) for training and assistance throughout
830 the NMR analyses. The authors also thank C.M. Jantzen, C.L. Trivelpiece, C.L. Crawford and
831 other developers for the development and maintenance of the ALTGLASS database.

832 **Funding**

833 This work was supported by EPSRC under an Industrial CASE award with the Nuclear
834 Decommissioning Authority (NDA) and Nuclear Waste Services (NWS) (Grant Ref:
835 EP/M507350).

836

References

[1] M.T. Harrison, Vitrification of High Level Waste in the UK, Procedia Mater. Sci. 7 (2014) 10–15. https://doi.org/10.1016/j.mspro.2014.10.003.

[2] S. Gin, A. Abdelouas, L.J. Criscenti, W.L. Ebert, K. Ferrand, T. Geisler, M.T. Harrison, Y. Inagaki, S. Mitsui, K.T. Mueller, J.C. Marra, C.G. Pantano, E.M. Pierce, J. V. Ryan, J.M. Schofield, C.I. Steefel, J.D. Vienna, An international initiative on long-term behavior of high-level nuclear waste glass, Mater. Today. 16 (2013) 243–248. https://doi.org/10.1016/j.mattod.2013.06.008.

[3] M. Le Grand, A.Y. Ramos, G. Calas, L. Galoisy, D. Ghaleb, F. Pacaud, Zinc environment in aluminoborosilicate glasses by Zn K-edge extended X-ray absorption fine structure spectroscopy, J. Mater. Res. 15 (2000) 2015–2019. https://doi.org/10.1557/JMR.2000.0289.

[4] E. Curti, J.L. Crovisier, G. Morvan, A.M. Karpoff, Long-term corrosion of two nuclear waste reference glasses (MW and SON68): A kinetic and mineral alteration study, Appl. Geochemistry. 21 (2006) 1152–1168. https://doi.org/10.1016/j.apgeochem.2006.03.010.

[5] G.S. Frankel, J.D. Vienna, J. Lian, X. Guo, S. Gin, S.H. Kim, J. Du, J. V. Ryan, J. Wang, W. Windl, C.D. Taylor, J.R. Scully, Recent Advances in Corrosion Science Applicable to Disposal of High-Level Nuclear Waste, Chem. Rev. (2021). https://doi.org/10.1021/acs.chemrev.0c00990.

[6] N.J. Cassingham, M.C. Stennett, P.A. Bingham, N.C. Hyatt, G. Aquilanti, The Structural Role of Zn in Nuclear Waste Glasses, Int. J. Appl. Glas. Sci. 2 (2011) 343–353. https://doi.org/10.1111/j.2041-1294.2011.00067.x.

[7] B.F. Dunnett, Review of the Development of UK High Level Waste Vitrified Product, Nexia Solutions report (06) 7926 Issue 4, 2007.

[8] M.T. Harrison, C.J. Steele, A.D. Riley, The effect on long term aqueous durability of variations in the composition of UK vitrified HLW product, Glas. Technol. Eur. J. Glas. Sci. Technol. Part A. 53 (2012) 211–216.

[9] A.R. Hall, J.T. Dalton, B. Hudson, J.A.C. Marples, Development and radiation stability of glasses for highly radioactive wastes, in: Management of radioactive wastes from the nuclear fuel cycle, 1976: pp. 3–14. https://doi.org/10.1016/0048-9697(78)90008-6.

[10] C. Magrabi, W. Smith, M.J. Larkin, Development of the glass formulation for the Windscale vitrification plant, in: Rad. Waste Mgt. and the Nucl. Fuel Cycle, 1987: pp. 85–106.

[11] A.J. Fisher, M.N.B. Imran, C. Mann, C. Gausse, R.J. Hand, N.C. Hyatt, C.L. Corkhill, Short communication: The dissolution of UK simulant vitrified high-level-waste in groundwater solutions, J. Nucl. Mater. 538 (2020) 1–7. https://doi.org/10.1016/j.jnucmat.2020.152245.

[12] C. Jégou, S. Narayanasamy, F. Angeli, Short communication on the Influence of the temperature between 30 and 70°C on the hydration of SON68 nuclear waste glass in a vapour phase, J. Nucl. Mater. 545 (2021) 152738. https://doi.org/10.1016/j.jnucmat.2020.152738.

[13] C. Carriere, P. Dillmann, S. Gin, D. Neff, L. Gentaz, F. Bruguier, I. Monnet, E. Gardes, M. Saheb, E. Foy, N. Nuns, A. Delanoë, J.J. Dynes, N. Michau, C. Martin, The fate of Si and Fe while nuclear glass alters with steel and clay, Npj Mater. Degrad. 5 (2021). https://doi.org/10.1038/s41529-021-00160-x.

[14] A.J. Fisher, M.T. Harrison, N.C. Hyatt, R.J. Hand, C.L. Corkhill, The dissolution of simulant UK Ca/Zn-modified nuclear waste glass : the effect of increased waste loading, MRS Adv. (2021) 1–8. https://doi.org/10.1557/s43580-021-00025-0.

[15] M.T. Harrison, The Effect of Composition on Short- and Long-term Durability of UK HLW Glass, Procedia Mater. Sci. 7 (2014) 186–192. https://doi.org/10.1016/j.mspro.2014.10.025.

[16] S. Gin, X. Beaudoux, F. Angeli, C. Jegou, N. Godon, Effect of composition on the short-term and long-term dissolution rates of ten borosilicate glasses of increasing complexity from 3 to 30 oxides, J. Non. Cryst. Solids. 358 (2012) 2559–2570. https://doi.org/10.1016/j.jnoncrysol.2012.05.024.

[17] S. Gin, P. Frugier, P. Jollivet, F. Bruguier, E. Curti, New Insight into the Residual Rate of Borosilicate Glasses: Effect of S/V and Glass Composition, Int. J. Appl. Glas. Sci. 4 (2013) 371–382. https://doi.org/10.1111/ijag.12048.

[18] F. Wang, N. Balasubramanya, Q. Qin, R.E. Youngman, P. Mukherjee, N. Stone-Weiss, A. Goel, Multiscale investigation of the mechanisms controlling the corrosion of borosilicate glasses in hyper-alkaline media, J. Phys. Chem. C. 124 (2020) 27542–27557. https://doi.org/10.1021/acs.jpcc.0c08691.

[19] H. Aréna, D. Rébiscoul, E. Garcès, N. Godon, Comparative effect of alkaline elements and calcium on alteration of International Simple Glass, Npj Mater. Degrad. 3 (2019) 1–11. https://doi.org/10.1038/s41529-019-0072-7.

[20] T.L. Goût, M.T. Harrison, I. Farnan, Impacts of lithium on Magnox waste glass dissolution, J. Non. Cryst. Solids. 517 (2019) 96–105. https://doi.org/10.1016/j.jnoncrysol.2019.04.040.

[21] N. Rajmohan, P. Frugier, S. Gin, Composition effects on synthetic glass alteration mechanisms: Part 1. Experiments, Chem. Geol. 279 (2010) 106–119. https://doi.org/10.1016/j.chemgeo.2010.10.010.

[22] S. Gin, J.-M. Delaye, F. Angeli, S. Schuller, Aqueous alteration of silicate glass: state of knowledge and perspectives, Npj Mater. Degrad. 5 (2021). https://doi.org/10.1038/s41529-021-00190-5.

[23] R. Bhattoo, S. Bishnoi, M. Zaki, N.M.A. Krishnan, Understanding the compositional control on electrical, mechanical, optical, and physical properties of inorganic glasses with interpretable machine learning, Acta Mater. 242 (2023) 118439. https://doi.org/10.1016/j.actamat.2022.118439.

[24] M. Zaki, S.R. Namireddy, T. Pittie, V. Bihani, S.R. Keshri, V. Venugopal, N.N. Gosvami, Jayadeva, N.M.A. Krishnan, Natural language processing-guided meta-analysis and structure factor database extraction from glass literature, J. Non-Crystalline Solids X. 15 (2022) 100103. https://doi.org/10.1016/j.nocx.2022.100103.

[25] X. Lu, L. Deng, J. Du, J.D. Vienna, Predicting boron coordination in multicomponent borate and borosilicate glasses using analytical models and machine learning, J. Non. Cryst. Solids. 553 (2021) 120490. https://doi.org/10.1016/j.jnoncrysol.2020.120490.

[26] S. Bishnoi, R. Ravinder, H.S. Grover, H. Kodamana, N.M.A. Krishnan, Scalable Gaussian processes for predicting the optical, physical, thermal, and mechanical properties of inorganic glasses with large datasets, Mater. Adv. 2 (2021) 477–487. https://doi.org/10.1039/d0ma00764a.

[27] D.R. Cassar, A.C.P.L.F. de Carvalho, E.D. Zanotto, Predicting glass transition temperatures using neural networks, Acta Mater. 159 (2018) 249–256. https://doi.org/10.1016/j.actamat.2018.08.022.

[28] D.R. Cassar, ViscNet: Neural network for predicting the fragility index and the temperature-dependency of viscosity, Acta Mater. 206 (2021) 116602. https://doi.org/10.1016/j.actamat.2020.116602.

[29] D.R. Cassar, G.G. Santos, E.D. Zanotto, Designing optical glasses by machine learning coupled with a genetic algorithm, Ceram. Int. 47 (2021) 10555–10564. https://doi.org/10.1016/j.ceramint.2020.12.167.

[30] D.R. Cassar, S.M. Mastelini, T. Botari, E. Alcobaça, A.C.P.L.F. de Carvalho, E.D. Zanotto, Predicting and interpreting oxide glass properties by machine learning using large datasets, Ceram. Int. 47 (2021) 23958–23972. https://doi.org/10.1016/j.ceramint.2021.05.105.

[31] Y. Minet, B. Bonin, S. Gin, P. Frugier, Analytic implementation of the GRAAL model: Application to a R7T7-type glass package in a geological disposal environment, J. Nucl. Mater. 404 (2010) 178–202. https://doi.org/10.1016/j.jnucmat.2010.07.015.

[32] P. Frugier, T. Chave, S. Gin, J.E. Lartigue, Application of the GRAAL model to leaching experiments with SON68 nuclear glass in initially pure water, J. Nucl. Mater. 392 (2009) 552–567. https://doi.org/10.1016/j.jnucmat.2009.04.024.

[33] P.C. Rieke, S. Kerisit, J. V. Ryan, J.J. Neeway, Adaptation of the GRAAL model of Glass Reactivity to accommodate non-linear diffusivity, J. Nucl. Mater. 512 (2018) 79–93. https://doi.org/10.1016/j.jnucmat.2018.09.058.

[34] S. Gin, X. Guo, J.-M. Delaye, F. Angeli, K. Damodaran, V. Testud, J. Du, S. Kerisit, S.H. Kim, Insights into the mechanisms controlling the residual corrosion rate of borosilicate glasses, Npj Mater. Degrad. 4 (2020) 41. https://doi.org/10.1038/s41529-020-00145-2.

[35] C. Lenting, O. Plümper, M. Kilburn, P. Guagliardo, M. Klinkenberg, T. Geisler, Towards a unifying mechanistic model for silicate glass corrosion, Npj Mater. Degrad. 2 (2018). https://doi.org/10.1038/s41529-018-0048-z.

[36] T. Han, N. Stone-Weiss, J. Huang, A. Goel, A. Kumar, Machine learning as a tool to design glasses with controlled dissolution for healthcare applications, Acta Biomater. 107 (2020) 286–298. https://doi.org/10.1016/j.actbio.2020.02.037.

[37] N.M. Anoop Krishnan, S. Mangalathu, M.M. Smedskjaer, A. Tandia, H. Burton, M. Bauchy, Predicting the dissolution kinetics of silicate glasses using machine learning, J. Non. Cryst. Solids. 487 (2018) 37–45. https://doi.org/10.1016/j.jnoncrysol.2018.02.023.

[38] H. Liu, T. Zhang, N.M. Anoop Krishnan, M.M. Smedskjaer, J. V. Ryan, S. Gin, M. Bauchy, Predicting the dissolution kinetics of silicate glasses by topology-informed machine learning, Npj Mater. Degrad. 3 (2019). https://doi.org/10.1038/s41529-019-0094-1.

[39] J.N.P. Lillington, T.L. Goût, M.T. Harrison, I. Farnan, Assessing static glass leaching predictions from large datasets using machine learning, J. Non. Cryst. Solids. 546 (2020) 120276. https://doi.org/10.1016/j.jnoncrysol.2020.120276.

[40] G. Hu, W. Pfingsten, Data-driven machine learning for disposal of high-level nuclear waste: A review, Ann. Nucl. Energy. 180 (2023) 109452. https://doi.org/10.1016/j.anucene.2022.109452.

[41] J.N.P. Lillington, T.L. Goût, M.T. Harrison, I. Farnan, Predicting radioactive waste glass dissolution with machine learning, J. Non. Cryst. Solids. 533 (2020) 119852. https://doi.org/10.1016/j.jnoncrysol.2019.119852.

[42] C.L. Trivelpiece, C.M. Jantzen, C.L. Crawford, Accelerated Leach Testing of GLASS: ALTGLASS Version 3.0, United States, 2016. https://doi.org/10.2172/1340201.

[43] C.M. Jantzen, C.L. Trivelpiece, C.L. Crawford, J.M. Pareizs, J.B. Pickett, Accelerated Leach Testing of GLASS (ALTGLASS): I. Informatics approach to high level waste glass gel formation and aging, Int. J. Appl. Glas. Sci. 8 (2017) 69–83. https://doi.org/10.1111/ijag.12262.

[44] Y. Gu, Q. Liao, F. Wang, J. Bin, Y. Wang, Y. Xu, H. Zhu, J. Zhou, Y. Luo, Y. Zhu, Effect of Li_2O substitution for Na_2O on the solubility and water durability of Mo in aluminoborosilicate glass, Int. J. Appl. Glas. Sci. (2021) 1–9. https://doi.org/10.1111/ijag.16114.

[45] A. Verney-Carron, S. Gin, P. Frugier, G. Libourel, Long-term modeling of alteration-transport coupling: Application to a fractured Roman glass, Geochim. Cosmochim. Acta. 74 (2010) 2291–2315. https://doi.org/10.1016/j.gca.2010.01.001.

[46] T. Chave, P. Frugier, S. Gin, A. Ayral, Glass-water interphase reactivity with calcium rich solutions, Geochim. Cosmochim. Acta. 75 (2011) 4125–4139. https://doi.org/10.1016/j.gca.2011.05.005.

[47] ASTM, Standard Test Methods for Determining Chemical Durability of Nuclear , Hazardous , and Mixed Waste Glasses and Multiphase Glass Ceramics : The Product Consistency Test (PCT) Designation: C1285-14, 2014. https://doi.org/10.1520/C1285-14.2.

[48] J.M. Roderick, D. Holland, A.P. Howes, C.R. Scales, Density-structure relations in mixed-alkali borosilicate glasses by ^{29}Si and ^{11}B MAS-NMR, J. Non. Cryst. Solids. 293–295 (2001) 746–751. https://doi.org/10.1016/S0022-3093(01)00784-0.

[49] A.J. Connelly, K.P. Travis, R.J. Hand, N.C. Hyatt, E. Maddrell, Composition-Structure Relationships in Simplified Nuclear Waste Glasses: 2. The Effect of ZrO_2 Additions, J. Am. Ceram. Soc. 94 (2011) 137–144. https://doi.org/10.1111/j.1551-2916.2010.04036.x.

[50] A.J. Connelly, R.J. Hand, P.A. Bingham, N.C. Hyatt, Mechanical properties of nuclear waste glasses, J. Nucl. Mater. 408 (2011) 188–193. https://doi.org/10.1016/j.jnucmat.2010.11.034.

[51] R. Short, Phase Separation and Crystallisation in UK HLW Vitrified Products, Procedia Mater. Sci. 7 (2014) 93–100. https://doi.org/10.1016/j.mspro.2014.10.013.

[52] R. Short, N. Gribble, A. Riley, Widening the envelope of UK HLW vitrification – Experimental studies with high waste loadings and new product formulations on a full scale non-active vitrification plant, Waste Manag. 2008. (2008) 1–11.

[53] W.J. Dell, P.J. Bray, S.Z. Xiao, ^{11}B NMR studies and structural modeling of $Na_2OB2O_3SiO_2$ glasses of high soda content, J. Non. Cryst. Solids. 58 (1983) 1–16. https://doi.org/10.1016/0022-3093(83)90097-2.

[54] B.G. Parkinson, D. Holland, M.E. Smith, C. Larson, J. Doerr, M. Affatigato, S.A. Feller, A.P. Howes, C.R. Scales, Quantitative measurement of Q^3 species in silicate and borosilicate glasses using Raman spectroscopy, J. Non. Cryst. Solids. 354 (2008) 1936–1942. https://doi.org/10.1016/j.jnoncrysol.2007.06.105.

[55] T. Nanba, M. Nishimura, Y. Miura, A theoretical interpretation of the chemical shift of ^{29}Si NMR peaks in alkali borosilicate glasses, Geochim. Cosmochim. Acta. 68 (2004) 5103–5111. https://doi.org/10.1016/j.gca.2004.05.042.

[56] K. Januchta, T. To, M.S. Bødker, T. Rouxel, M.M. Smedskjaer, Elasticity, hardness, and fracture toughness of sodium aluminoborosilicate glasses, J. Am. Ceram. Soc. 102 (2019) 4520–4537. https://doi.org/10.1111/jace.16304.

[57] K.P. Jochum, U. Nohl, K. Herwig, E. Lammel, B. Stoll, A.W. Hofmann, GeoReM: A New Geochemical Database for Reference Materials and Isotopic Standards, Geostand. Geoanalytical Res. 29 (2005) 333–338. https://doi.org/10.1111/j.1751-908x.2005.tb00904.x.

[58] M. Fournier, A. Ull, E. Nicoleau, Y. Inagaki, M. Odorico, P. Frugier, S. Gin, Glass dissolution rate measurement and calculation revisited, J. Nucl. Mater. 476 (2016) 140–154. https://doi.org/10.1016/j.jnucmat.2016.04.028.

[59] B.E. Scheetz, M.P. Freeborn, D.K. Smith, C. Anderson, M. Zolensky, W.B. White, The role of boron in monitoring the leaching of borosilicate waste forms, Mater. Res. Soc. Symp. - Proc. 44 (1984) 129–134.

[60] E.M. Pierce, E.L. Richards, A.M. Davis, L.R. Reed, E.A. Rodriguez, Aluminoborosilicate waste glass dissolution under alkaline conditions at 40°C: Implications for a chemical affinity-based rate equation, Environ. Chem. 5 (2008) 73–85. https://doi.org/10.1071/EN07058.

[61] J.P. Icenhower, D.M. Strachan, B.P. McGrail, R.D. Scheele, E.A. Rodriguez, J.L. Steele, V.L. Legore, Dissolution kinetics of pyrochlore ceramics for the disposition of plutonium, Am. Mineral. 91 (2006) 39–53. https://doi.org/10.2138/am.2006.1709.

[62] B.P. McGrail, J.P. Icenhower, D.K. Shuh, P. Liu, J.G. Darab, D.R. Baer, S. Thevuthasen, V. Shutthanandan, M.H. Engelhard, C.H. Booth, P. Nachimuthu, The structure of Na_2O-Al_2O_3-SiO_2 glass: Impact on sodium ion exchange in H_2O and D_2O, J. Non. Cryst. Solids. 296 (2001) 10–26. https://doi.org/10.1016/S0022-3093(01)00890-0.

[63] N. Stone-Weiss, R.E. Youngman, R. Thorpe, N.J. Smith, E.M. Pierce, A. Goel, An insight into the corrosion of alkali aluminoborosilicate glasses in acidic environments, Phys. Chem. Chem. Phys. 22 (2020) 1881–1896. https://doi.org/10.1039/c9cp06064b.

[64] D. Wolff-Boenisch, S.R. Gislason, E.H. Oelkers, C. V. Putnis, The dissolution rates of natural glasses as a function of their composition at pH 4 and 10.6, and temperatures from 25 to 74°C, Geochim. Cosmochim. Acta. 68 (2004) 4843–4858. https://doi.org/10.1016/j.gca.2004.05.027.

[65] T. Chave, P. Frugier, A. Ayral, S. Gin, Solid state diffusion during nuclear glass residual alteration in solution, J. Nucl. Mater. 362 (2007) 466–473. https://doi.org/10.1016/j.jnucmat.2007.01.095.

[66] P. Frugier, S. Gin, Y. Minet, T. Chave, B. Bonin, N. Godon, J.E. Lartigue, P. Jollivet, A. Ayral, L. De Windt, G. Santarini, SON68 nuclear glass dissolution kinetics: Current state of knowledge and basis of the new GRAAL model, J. Nucl. Mater. 380 (2008) 8–21. https://doi.org/10.1016/j.jnucmat.2008.06.044.

[67] C. Jégou, S. Gin, F. Larché, Alteration kinetics of a simplified nuclear glass in an aqueous medium: Effects of solution chemistry and of protective gel properties on diminishing the alteration rate, J. Nucl. Mater. 280 (2000) 216–229. https://doi.org/10.1016/S0022-3115(00)00039-8.

[68] D.L. Parkhurst, C.A.J. Appelo, Description of Input and Examples for PHREEQC Version 3 — A Computer Program for Speciation , Batch-Reaction , One-Dimensional Transport , and Inverse Geochemical Calculations. U.S. Geological Survey Techniques and Methods, book 6, chapter A43, 497 p., U.S. Geol. Surv. Tech. Methods, B. 6, Chapter A43. (2013) 6-43A. https://doi.org/10.1016/0029-6554(94)90020-5.

[69] E. Giffaut, M. Grivé, P. Blanc, P. Vieillard, E. Colàs, H. Gailhanou, S. Gaboreau, N. Marty, B. Madé, L. Duro, Andra thermodynamic database for performance assessment: ThermoChimie, Appl. Geochemistry. 49 (2014) 225–236. https://doi.org/10.1016/j.apgeochem.2014.05.007.

[70] T. Wolery, S. Daveler, EQ6, a computer program for reaction path modeling of aqueous geochemical systems: Theoretical manual, users guide, and related documentation (Version 7.0); Part 4. UCRL-MA-110662-Pt. 4, 1992.

[71] J. Ball, D. Nordstrom, User's manual for WATEQ4F, with revised thermodynamic database and test cases for calculating speciation of major, trace, and redox elements in natural waters, 1991.

[72] K. Bennington, M. Ferrante, J. Stuve, Thermodynamic properties of two lithium silicates (Li_2SiO_3 and $Li_2Si_2O_5$), 1976.

[73] D.M. Strachan, J.J. Neeway, Effects of alteration product precipitation on glass dissolution, Appl. Geochemistry. 45 (2014) 144–157. https://doi.org/10.1016/j.apgeochem.2014.03.013.

[74] M. Voigt, C. Marieni, A. Baldermann, I.M. Galeczka, D. Wolff-Boenisch, E.H. Oelkers, S.R. Gislason, An experimental study of basalt–seawater–CO_2 interaction at 130 °C, Geochim. Cosmochim. Acta. 308 (2021) 21–41. https://doi.org/10.1016/j.gca.2021.05.056.

[75] J. Rumble, Mean Surface Temperature and Pressure and Atmospheric Composition of the Major Planets and Pluto, in: CRC Handb. Chem. Phys., 102nd ed., 2021.

[76] P. Van Iseghem, M. Aertsens, S. Gin, D. Deneele, B. Grambow, D. Strachan, P. McGrail, G. Wicks, Glamor - or how we achieved a common understanding on the decrease of glass dissolution kinetics, Ceram. Trans. 207 (2009) 115–126.

[77] B. Grambow, A general rate equation for nuclear waste glass corrosion, Mater. Res. Soc. Symp. - Proc. 44 (1985) 15–27.

[78] I. Techer, T. Advocat, J. Lancelot, J.M. Liotard, Dissolution kinetics of basaltic glasses: Control by solution chemistry and protective effect of the alteration film, Chem. Geol. 176 (2001) 235–263. https://doi.org/10.1016/S0009-2541(00)00400-9.

[79] S. Gin, A.H. Mir, A. Jan, J.-M.M. Delaye, E. Chauvet, Y. De Puydt, A. Gourgiotis, S.N. Kerisit, A General Mechanism for Gel Layer Formation on Borosilicate Glass under Aqueous Corrosion, J. Phys. Chem. C. 124 (2020) 5132–5144. https://doi.org/10.1021/acs.jpcc.9b10491.

[80] W.L. Bourcier, D.W. Peiffer, K.G. Knauss, K.D. McKeegan, D.K. Smith, A Kinetic Model for Borosilicate Glass Dissolution Based on the Dissolution Affinity of a Surface Alteration Layer, MRS Proc. 176 (1990) 209–216. https://doi.org/10.1557/proc-176-209.

[81] I. Galeczka, D. Wolff-Boenisch, E.H. Oelkers, S.R. Gislason, An experimental study of basaltic glass-H_2O-CO_2 interaction at 22 and 50°C: Implications for subsurface storage of CO_2, Geochim. Cosmochim. Acta. 126 (2014) 123–145. https://doi.org/10.1016/j.gca.2013.10.044.

[82] B. Parruzot, P. Jollivet, D. Rebiscoul, S. Gin, Long-term alteration of basaltic glass: Mechanisms and rates, Geochim. Cosmochim. Acta. 154 (2015) 28–48. https://doi.org/10.1016/j.gca.2014.12.011.

[83] C.M. Jantzen, C.L. Trivelpiece, C.L. Crawford, Accelerated Leach Testing of GLASS (ALTGLASS Version 4.0), United States, 2019. https://doi.org/10.2172/1581230.

[84] J. Wainer, G. Cawley, Nested cross-validation when selecting classifiers is overzealous for most practical applications, Expert Syst. Appl. 182 (2021) 115222. https://doi.org/10.1016/j.eswa.2021.115222.

[85] D. Krstajic, L.J. Buturovic, D.E. Leahy, S. Thomas, Cross-validation pitfalls when selecting and assessing regression and classification models, J. Cheminform. 6 (2014) 1–15. https://doi.org/10.1186/1758-2946-6-10.

[86] D. Massiot, F. Fayon, M. Capron, I. King, S. Le Calvé, B. Alonso, J.O. Durand, B. Bujoli, Z. Gan, G. Hoatson, Modelling one- and two-dimensional solid-state NMR spectra, Magn. Reson. Chem. 40 (2002) 70–76. https://doi.org/10.1002/mrc.984.

[87] F. Angeli, T. Charpentier, D. De Ligny, C. Cailleteau, Boron speciation in soda-lime borosilicate glasses containing zirconium, J. Am. Ceram. Soc. 93 (2010) 2693–2704. https://doi.org/10.1111/j.1551-2916.2010.03771.x.

[88] F. Angeli, O. Villain, S. Schuller, T. Charpentier, D. De Ligny, L. Bressel, L. Wondraczek, Effect of temperature and thermal history on borosilicate glass structure, Phys. Rev. B - Condens. Matter Mater. Phys. 85 (2012). https://doi.org/10.1103/PhysRevB.85.054110.

[89] F. Angeli, T. Charpentier, P. Jollivet, D. de Ligny, M. Bergler, A. Veber, S. Gin, H. Li, Effect of thermally induced structural disorder on the chemical durability of International Simple Glass, Npj Mater. Degrad. 2 (2018) 1–11. https://doi.org/10.1038/s41529-018-0052-3.

[90] L.-S. Du, J.F. Stebbins, Site Preference and Si/B Mixing in Mixed-Alkali Borosilicate Glasses: A High-Resolution ^{11}B and ^{17}O NMR Study, Chem. Mater. 15 (2003) 3913–3921. https://doi.org/10.1021/cm034427r.

[91] E.M. Pierce, L.R. Reed, W.J. Shaw, B.P. McGrail, J.P. Icenhower, C.F. Windisch, E.A. Cordova, J. Broady, Experimental determination of the effect of the ratio of B/Al on glass dissolution along the nepheline ($NaAlSiO_4$)-malinkoite ($NaBSiO_4$) join, Geochim. Cosmochim. Acta. 74 (2010) 2634–2654. https://doi.org/10.1016/j.gca.2009.09.006.

[92] J. Hopf, S.N. Kerisit, F. Angeli, T. Charpentier, J.P. Icenhower, B.P. McGrail, C.F. Windisch, S.D. Burton, E.M. Pierce, Glass-water interaction: Effect of high-valence cations on glass structure and chemical durability, Geochim. Cosmochim. Acta. 181 (2016) 54–71. https://doi.org/10.1016/j.gca.2016.02.023.

[93] T.L. Goût, M.T. Harrison, I. Farnan, Relating Magnox and international waste glasses, J. Non. Cryst. Solids. 524 (2019) 119647. https://doi.org/10.1016/j.jnoncrysol.2019.119647.

[94] P.P. Man, Quadrupole Couplings in Nuclear Magnetic Resonance, General, in: Encycl. Anal. Chem. Appl. Theory Instrum., 2006. https://doi.org/https://doi.org/10.1002/9780470027318.a6111.

[95] A. Ledieu, F. Devreux, P. Barboux, L. Sicard, O. Spalla, Leaching of borosilicate glasses. I. Experiments, J. Non. Cryst. Solids. 343 (2004) 3–12. https://doi.org/10.1016/j.jnoncrysol.2004.06.006.

[96] L. Trotignon, J.C. Petit, G. Della Mea, J.C. Dran, The compared aqueous corrosion of four simple borosilicate glasses: Influence of Al, Ca and Fe on the formation and nature of secondary phases, J. Nucl. Mater. 190 (1992) 228–246. https://doi.org/10.1016/0022-3115(92)90088-3.

[97] L. Breiman, Random Forests, Mach. Learn. 45 (2021) 5–32.

[98] E. Vernaz, S. Gin, Apparent Solubility Limit of Nuclear Glass, Mater. Res. Soc. Symp. - Proc. 663 (2001) 1–9.

[99] P. Rautiyal, G. Gupta, R. Edge, L. Leay, A. Daubney, M.K. Patel, A.H. Jones, P.A. Bingham, Gamma irradiation-induced defects in borosilicate glasses for high-level radioactive waste immobilisation, J. Nucl. Mater. 544 (2021) 152702. https://doi.org/10.1016/j.jnucmat.2020.152702.

[100] O.N. Koroleva, L.A. Shabunina, V.N. Bykov, Structure of borosilicate glass according to raman spectroscopy data, Glas. Ceram. (English Transl. Steklo i Keramika). 67 (2011) 340–342. https://doi.org/10.1007/s10717-011-9293-0.

[101] B.G. Parkinson, D. Holland, M.E. Smith, A.P. Howes, C.R. Scales, The effect of oxide additions on medium-range order structures in borosilicate glasses, J. Phys. Condens. Matter. 19 (2007) 415114. https://doi.org/10.1088/0953-8984/19/41/415114.

[102] D. Manara, A. Grandjean, D.R. Neuville, Advances in understanding the structure of borosilicate glasses: A raman spectroscopy study, Am. Mineral. 94 (2009) 777–784. https://doi.org/10.2138/am.2009.3027.

[103] T. Furukawa, W.B. White, Raman spectroscopic investigation of sodium borosilicate glass structure, J. Mater. Sci. 16 (1981) 2689–2700. https://doi.org/10.1007/BF00552951.

[104] G. Karakurt, A. Abdelouas, J.P. Guin, M. Nivard, T. Sauvage, M. Paris, J.F. Bardeau, Understanding of the mechanical and structural changes induced by alpha particles and heavy ions in the French simulated nuclear waste glass, J. Nucl. Mater. 475 (2016) 243–254. https://doi.org/10.1016/j.jnucmat.2016.04.022.

[105] A.H. Mir, I. Monnet, B. Boizot, C. Jégou, S. Peuget, Electron and electron-ion sequential irradiation of borosilicate glasses: Impact of the pre-existing defects, J. Nucl. Mater. 489 (2017) 91–98. https://doi.org/10.1016/j.jnucmat.2017.03.047.

[106] R.K. Biswas, P. Khan, S. Mukherjee, A.K. Mukhopadhyay, J. Ghosh, K. Muraleedharan, Study of short range structure of amorphous Silica from PDF using Ag radiation in laboratory XRD system, RAMAN and NEXAFS, J. Non. Cryst. Solids. 488 (2018) 1–9. https://doi.org/10.1016/j.jnoncrysol.2018.02.037.

[107] C. Lenting, T. Geisler, Corrosion of ternary borosilicate glass in acidic solution studied in operando by fluid-cell Raman spectroscopy, Npj Mater. Degrad. 37 (2021) 1–9. https://doi.org/10.1038/s41529-021-00182-5.

[108] N. Shibata, M. Horigudhi, T. Edahiro, Raman spectra of binary high-silica glasses and fibers containing GeO_2, P_2O_5 and B_2O_3, J. Non. Cryst. Solids. 45 (1981) 115–126. https://doi.org/10.1016/0022-3093(81)90096-X.

[109] B.O. Mysen, L.W. Finger, D. Virgo, F.A. Seifert, Curve-fitting of Raman spectra of silicate glasses., Am. Mineral. 67 (1982) 686–695.

[110] M. Collin, M. Fournier, T. Charpentier, M. Moskura, S. Gin, Impact of alkali on the passivation of silicate glass, Npj Mater. Degrad. 2 (2018) 1–10. https://doi.org/10.1038/s41529-018-0036-3.

[111] M. Collin, M. Fournier, P. Frugier, T. Charpentier, M. Moskura, L. Deng, M. Ren, J. Du, S. Gin, Structure of International Simple Glass and properties of passivating layer formed in circumneutral pH conditions, Npj Mater. Degrad. 2 (2018) 1–12. https://doi.org/10.1038/s41529-017-0025-y.

[112] Y. Huang, Vibrational spectroscopic studies of layered silicates, Chem. Mater. 11 (1999) 1210–1217. https://doi.org/10.1021/cm980403m.

[113] H. Aréna, R. Podor, H.P. Brau, J. Nelayah, N. Godon, M. Cabié, E. Garcès, C. Mansas, D. Rébiscoul, Characterization of the boron profile and coordination in altered glass layers by EEL spectroscopy, Micron. 141 (2021). https://doi.org/10.1016/j.micron.2020.102983.

[114] K.A. Murphy, N.M. Washton, J. V. Ryan, C.G. Pantano, K.T. Mueller, Solid-state NMR examination of alteration layers on nuclear waste glasses, J. Non. Cryst. Solids. 369 (2013) 44–54. https://doi.org/10.1016/j.jnoncrysol.2013.03.021.

[115] H. Koller, G. Engelhardt, A.P.M. Kentgens, J. Sauer, ^{23}Na NMR spectroscopy of solids: Interpretation of quadrupole interaction parameters and chemical shifts, J. Physial Chem. 98 (1994) 1544–1551. https://doi.org/10.1021/j100057a004.

[116] G.G. Almond, R.K. Harris, K.R. Franklin, P. Graham, A ^{23}Na NMR study of hydrous layered silicates, J. Mater. Chem. 6 (1996) 843–847. https://doi.org/10.1039/jm9960600843.

[117] J.M. Rojo, E. Ruiz-Hitzky, J. Sanz, Proton-Sodium Exchange in Magadiite. Spectroscopic Study (NMR, IR) of the Evolution of Interlayer OH Groups, Inorg. Chem. 27 (1988) 2785–2790. https://doi.org/10.1021/ic00289a009.

[118] T. Charpentier, S. Ispas, M. Profeta, F. Mauri, C.J. Pickard, First-Principles Calculation of ^{17}O, ^{29}Si, and ^{23}Na NMR Spectra of Sodium Silicate Crystals and Glasses, J. Phys. Chem. B. 108 (2004) 4147–4161. https://doi.org/10.1021/jp0367225.

[119] A.R. Jones, R. Winter, P. Florian, D. Massiot, Tracing the reactive melting of glass-forming silicate batches by in situ23Na NMR, J. Phys. Chem. B. 109 (2005) 4324–4332. https://doi.org/10.1021/jp045705s.

[120] D. Heidemann, C. Hubert, W. Schwieger, P. Grabner, K.-H. Bergk, P. Sarv, ^{29}Si- und ^{23}Na-Festkorper-MAS-NMR-Untersuchungen an Modifikationen des $Na_2Si_2O_5$, Zeitschrift Fur Anorg. Und Allg. Chemie. 617 (1992) 169–177. https://doi.org/10.1002/zaac.19926170129.

[121] B. Parruzot, J. V. Ryan, A.M. Lines, S.A. Bryan, J.J. Neeway, S. Chatterjee, C.D. Lukins, A.J. Casella, Method for the in situ Measurement of pH and Alteration Extent for Aluminoborosilicate Glasses Using Raman Spectroscopy, Anal. Chem. 90 (2018) 11812–11819. https://doi.org/10.1021/acs.analchem.8b00960.

[122] J. V. Ryan, B. Parruzot, A.M. Lines, S.A. Bryan, L.M. Seymour, J.F. Bonnett, R.K. Motkuri, In-situ monitoring of seeded and unseeded stage III corrosion using Raman spectroscopy, Npj Mater. Degrad. 3 (2019) 1–7. https://doi.org/10.1038/s41529-019-0095-0.

[123] C.L. Corkhill, C. Mann, J.R. Eskelsen, D.N. Leonard, L.M. Mottram, M.C. Stennett, J.M.S. Ayling, C.L. Thorpe, M.R. Cole, S. Nicholas, R. Tappero, E.M. Pierce, Surface interfacial analysis of simulant high level nuclear waste glass dissolved in synthetic cement solutions, Npj Mater. Degrad. 6 (2022). https://doi.org/10.1038/s41529-022-00279-5.

[124] A.J. Mallette, J.T. Reiser, G. Mpourmpakis, R.K. Motkuri, J.J. Neeway, J.D. Rimer, The effect of metals on zeolite crystallization kinetics with relevance to nuclear waste glass corrosion, Npj Mater. Degrad. 7 (2023) 4. https://doi.org/10.1038/s41529-022-00310-9.

[125] J. Crum, J. Reiser, B. Parruzot, J. Neeway, J. Bonnett, S. Kerisit, S. Cooley, J. Ryan, G. Smith, R. Asmussen, Seeded Stage III Glass Dissolution Behavior of a Statistically Designed Glass Matrix, 2021. https://doi.org/10.1111/jace.17823.

[126] B. Parruzot, J. V Crum, J.T. Reiser, J.J. Neeway, S.N. Kerisit, R.C. Daniel, J.F. Bonnett, R.A. Reyes, L.M. Seymour, C.A. Burns, J. V Ryan, G.L. Smith, R.M. Asmussen, Effect of zeolite type, temperature, and pH on Stage III glass alteration behavior for two nuclear waste glasses, J. Nucl. Mater. (2022) 153717. https://doi.org/10.1016/j.jnucmat.2022.153717.

[127] J.J. Neeway, B.P. Parruzot, J.F. Bonnett, J.T. Reiser, S.N. Kerisit, J. V. Ryan, J. V. Crum, Acceleration of glass alteration rates induced by zeolite seeds at controlled pH, Appl. Geochemistry. 113 (2020) 104515. https://doi.org/10.1016/j.apgeochem.2019.104515.

[128] B.C. Bunker, Molecular mechanisms for corrosion of silica and silicate glasses, J. Non. Cryst. Solids. 179 (1994) 300–308. https://doi.org/10.1016/0022-3093(94)90708-0.

[129] C. Le Losq, D.R. Neuville, W. Chen, P. Florian, D. Massiot, Z. Zhou, G.N. Greaves, Percolation channels: A universal idea to describe the atomic structure and dynamics of glasses and melts, Sci. Rep. 7 (2017) 1–12. https://doi.org/10.1038/s41598-017-16741-3.

[130] M. Kinoshita, M. Harada, Y. Sato, Y. Hariguchi, Percolation Phenomenon for Dissolution of Sodium Borosilicate Glasses in Aqueous Solutions, J. Am. Ceram. Soc. 74 (1991) 783–787. https://doi.org/10.1111/j.1151-2916.1991.tb06925.x.

[131] B. Vessal, G.N. Greaves, P.T. Marten, A. V. Chadwick, R. Mole, S. Houde-Walter, Cation microsegregation and ionic mobility in mixed alkali glasses, Nature. 356 (1992) 504–506. https://doi.org/10.1038/356504a0.

[132] C. Cailleteau, C. Weigel, A. Ledieu, P. Barboux, F. Devreux, On the effect of glass composition in the dissolution of glasses by water, J. Non. Cryst. Solids. 354 (2008) 117–123. https://doi.org/10.1016/j.jnoncrysol.2007.07.063.

[133] F. Devreux, A. Ledieu, P. Barboux, Y. Minet, Leaching of borosilicate glasses. II. Model and Monte-Carlo simulations, J. Non. Cryst. Solids. 343 (2004) 13–25. https://doi.org/10.1016/j.jnoncrysol.2004.06.007.

[134] G.N. Greaves, EXAFS, glass structure and diffusion, Philos. Mag. B Phys. Condens. Matter; Stat. Mech. Electron. Opt. Magn. Prop. 60 (1989) 793–800. https://doi.org/10.1080/13642818908209743.

[135] M.I. Ojovan, A. Pankov, W.E. Lee, The ion exchange phase in corrosion of nuclear waste glasses, J. Nucl. Mater. 358 (2006) 57–68. https://doi.org/10.1016/j.jnucmat.2006.06.016.

[136] G.B. Alexander, W.M. Heston, R.K. Iler, The solubility of amorphous silica in water, J. Phys. Chem. 58 (1954) 453–455. https://doi.org/10.1021/j150516a002.

[137] Y. Linard, I. Yamashita, T. Atake, J. Rogez, P. Richet, Thermochemistry of nuclear waste glasses: An experimental determination, J. Non. Cryst. Solids. 286 (2001) 200–209. https://doi.org/10.1016/S0022-3093(01)00529-4.

[138] T. Ducasse, A. Gourgiotis, E. Pringle, F. Moynier, P. Frugier, P. Jollivet, S. Gin, Alteration of synthetic basaltic glass in silica saturated conditions: Analogy with nuclear glass, Appl. Geochemistry. 97 (2018) 19–31. https://doi.org/10.1016/j.apgeochem.2018.08.001.

[139] S. Gin, P. Jollivet, M. Fournier, F. Angeli, P. Frugier, T. Charpentier, Origin and consequences of silicate glass passivation by surface layers, Nat. Commun. 6 (2015) 6360. https://doi.org/10.1038/ncomms7360.

[140] T. Geisler, L. Dohmen, C. Lenting, M.B.K. Fritzsche, Real-time in situ observations of reaction and transport phenomena during silicate glass corrosion by fluid-cell Raman spectroscopy, Nat. Mater. 18 (2019) 342–348. https://doi.org/10.1038/s41563-019-0293-8.

[141] T.L. Goût, M.T. Harrison, I. Farnan, Evaluating the temperature dependence of Magnox waste glass dissolution, J. Non. Cryst. Solids. 518 (2019) 75–84. https://doi.org/10.1016/j.jnoncrysol.2019.05.017.